

Depth-Estimation and Seabed-Visualization Techniques for Airborne Laser Bathymetry

by

Wei Cheng

B.Sc., National Tsing Hua University, 1991

A Thesis Submitted in Partial Fulfillment of the
Requirements for the Degree of

MASTER OF APPLIED SCIENCE

in the Department of Electrical and Computer Engineering


We accept this thesis as conforming
to the required standard



Dr. A. Antoniou, Co-supervisor (Dept. of Elect. and Comp. Eng.)




Dr. W.-S. Lu, Co-supervisor (Dept. of Elect. and Comp. Eng.)



Dr. P. Agathoklis, Departmental Member (Dept. of Elect. and Comp. Eng.)



Dr. S. Dost, Outside Member (Dept. of Mech. Eng.)



Dr. D. Shpak, External Examiner (Dept. of Eng., Royal Roads Military College)

©WEI CHENG, 1995

University of Victoria

All rights reserved. The thesis may not be reproduced in whole or in part,
by photocopying or other means, without the permission of the author.

Supervisors: Drs. A. Antoniou and W.-S. Lu.

Abstract

Several techniques for the efficient processing of bathymetric data are developed. First, the characteristics of bathymetric signals are analyzed in both time domain and frequency domain. In the time-domain analysis, a bathymetric signal is characterized by three components that represent the blue-green surface reflection, volume backscatter, and bottom reflection. The characterization of the waveform facilitates decomposition of the waveform and renders the depth estimation reliable and physically meaningful. Recursive computational schemes for the evaluation of the signal model are derived. Our simulations have demonstrated that these recursive schemes can be used in optimization-based depth estimation algorithms with reduced computation complexity. In the frequency-domain analysis, the short-time discrete Fourier transform (STDFT) of the signal is used as a tool in the study of sea-depth estimation. In particular, we show that the STDFT evaluated at zero frequency provides an enhanced signal profile from which accurate estimates of sea depth can be obtained.

In the second part of the thesis, noise filtering techniques for obtaining improved 2-D seabed topography of coastal shallow waters are investigated. The characteristics of the noise with which the bathymetric signals are contaminated are studied. A simple, yet efficient, method for regularizing irregularly spaced data is developed. Then a 2-D noise filtering algorithm based on the use of local statistics of depth

measurements is described and applied to the data. The aforementioned processing involves only a small window of data surrounding the grid point being processed; consequently, the proposed algorithm can be implemented in real or quasi-real time.

Examiners:

[Redacted]

Dr. A. Antoniou, Co-supervisor (Dept. of Elect. and Comp. Eng.)

[Redacted]

Dr. W.-S. Lu, Co-supervisor (Dept. of Elect. and Comp. Eng.)

[Redacted]

Dr. P. Agathoklis, Departmental Member (Dept. of Elect. and Comp. Eng.)

[Redacted]

Dr. S. Dost, Outside Member (Dept. of Mech. Eng.)

[Redacted]

Dr. D. Shpak, External Examiner (Dept. of Eng., Royal Roads Military College)

To my parents and grandmother

Acknowledgements

The author would like to thank his supervisors, Professors A. Antoniou and W.-S. Lu of the Department of Electrical and Computer Engineering, for their encouragement, patience and advice during the course of this research, and for their help in the preparation of this thesis.

Financial assistance provided by Professors A. Antoniou and W.-S. Lu from research grants from the Natural Science and Engineering Research Council of Canada is also gratefully acknowledged.

The assistance rendered by Terra Surveys Ltd. by providing bathymetric field data for this project is fully appreciated. I also wish to express my appreciation to Mr. Rick Quinn and Dr. Hui-Ping Wang of Terra Surveys in this regard.

The initial stage of assistance from Dr. Henry Wong in terms of interpretation and analysis of bathymetric waveforms is also greatly appreciated.

Contents

Abstract	ii
Dedication	v
Acknowledgements	vi
Contents	vii
List of Tables	xii
List of Figures	xv
List of Abbreviations	xvi
1 Introduction	1
1.1 Airborne Laser Bathymetry	1

1.2	Historic Review of Bathymetry	2
1.2.1	Laser Bathymetry versus Acoustic Bathymetry	2
1.2.2	Development of Bathymetric Systems in Australia, Canada, and the US	5
1.3	Description of the LARSEN 500 Airborne Laser Bathymeter	10
1.3.1	The System	10
1.3.2	The Signals	11
1.3.3	Operational Considerations	12
1.3.4	The Laser Source	15
1.3.5	Eye Safety	17
1.3.6	System Design and Parameterization	18
1.3.7	Signal Processing	23
1.4	Optical Properties of Water	25
1.4.1	Secchi Depth	25
1.4.2	Diffuse Attenuation Coefficient	26
1.4.3	Beam Attenuation Coefficient	26
1.4.4	Interrelationships of the Parameters	27
1.5	Outline of the Main Results of the Thesis	28

2	One-Dimensional Processing of Bathymetric Data	30
2.1	Bathymetric Signals	30
2.2	The Discrete Fourier Transform	31
2.2.1	The z Transform	32
2.2.2	The Continuous-Time Fourier Transform	32
2.2.3	Short-time Discrete Fourier Transform	33
2.3	The STDFT	34
2.3.1	Definitions and Properties	34
2.4	Application of the STDFT to Bathymetric Signals	36
2.4.1	Evaluation of STDFT	41
2.5	Peak Identification	42
2.5.1	Differentiation of STDFT Spectrum	42
2.6	Conclusions	46
3	Characterization and Decomposition of Bathymetric Waveforms	48
3.1	Preprocessing	48
3.2	Characterization of Waveforms	49
3.3	Characterization of Surface Reflection	52

3.4	Characterization of Volume Backscatter	54
3.5	Characterization of Bottom Reflection	55
3.6	Recursive Computation of the Modeling Functions	56
3.6.1	Recursive Computation of the Surface Reflection	56
3.6.2	Recursive Computation of Bottom Reflection	59
3.6.3	Simulation Results	60
3.7	Optimization	61
3.7.1	The BFGS Optimization Method	62
3.8	Simulation Results	64
3.9	Conclusions	70
4	Two-Dimensional Processing of Bathymetric Topography	71
4.1	Introduction	71
4.2	Preprocessing	72
4.2.1	Data Segmentation	72
4.2.2	Data Interpolation	74
4.3	Additive Noise Filtering	79
4.4	Conclusions	82

<i>CONTENTS</i>	xi
5 Conclusions	83
5.1 Results of the Thesis	84
5.2 Future Studies	84
Bibliography	86
Appendix A - MATLAB Programs for Chapter 2	89
Appendix B - MATLAB Programs for Chapter 3	99
Appendix C - MATLAB Programs for Chapter 4	128

List of Tables

1.1	Maximum permissible exposure for the eye	18
2.1	Peak Locations v.s. STDFT window length (L) (5 cases)	47
3.1	Constants in the polynomial approximation for $I(z)$ in (3.5)	54
3.2	Computation complexity: recursive versus direct	61
3.3	Simulation results of several waveforms by waveform decomposition .	69

List of Figures

1.1	Laser beam geometry and receiver's field-of-view.	11
1.2	A typical bathymetric waveform. I: infrared surface reflection; II: blue-green surface reflection; III: volume backscatter; IV: bottom re- flection.	13
1.3	Information manipulation and processing.	24
2.1	Presentation of a bathymetric signal.	31
2.2	A typical waveform and its DFT spectrum (a) Original waveform (b) DFT of the waveform.	38
2.3	Spectrogram (normalized by the window length L) of the waveform in Figure 2.2 (a).	39

2.4 Cross-sections of the spectrogram in Figure 2.3 at some frequency components. The dotted line represents the original waveform and the solid line is the spectrogram plot. (a) $\omega_k = 0$ (b) $\omega_k = \pi$ (c) $\omega_k = \pi/(\text{window length})$ (d) $\omega_k = 2\pi-\pi/(\text{window length})$ 40

2.5 Comparison of STDFT of various window lengths with original waveform. The dotted line presents the original waveform and the solid line is the STDFT. (a) STDFT of window length 3 (b) STDFT of window length 7 (c) STDFT of window length 11 (d) STDFT of window length 15. 43

2.6 The original waveforms of the five cases used for demonstration of depth estimation by spectrogram. 45

3.1 Waveform decomposition of bathymetric data. (a) and (c) Actual bathymetric waveforms, (b) and (d) the dotted line is the blue-green surface reflection, the dashed line is volume backscatter, the solid line is bottom reflection, and the dashdot line is the smoothed waveform using a 12th-order FIR filter. 65

3.2 Waveform decomposition of bathymetric data. (a) and (c) Actual bathymetric waveforms, (b) and (d) the dotted line is the blue-green surface reflection, the dashed line is volume backscatter, the solid line is bottom reflection, and the dashdot line is the smoothed waveform using a 12th-order FIR filter. 66

3.3 Waveform decomposition of bathymetric data. (a) and (c) Actual bathymetric waveforms, (b) and (d) the dotted line is the blue-green surface reflection, the dashed line is volume backscatter, the solid line is bottom reflection, and the dashdot line is the smoothed waveform using a 12th-order FIR filter. 67

3.4 Waveform decomposition of bathymetric data. (a) and (c) Actual bathymetric waveforms, (b) and (d) the dotted line is the blue-green surface reflection, the dashed line is volume backscatter, the solid line is bottom reflection, and the dashdot line is the smoothed waveform using a 12th-order FIR filter. 68

4.1 Scattering sounding pattern. 73

4.2 Formation of regularly spaced data. 75

4.3 Contour map of reconstructed seabed topography by interpolation. . . 78

4.4 Contour map of filtered topography. 81

List of Abbreviations

1-D	one-dimensional
2-D	two-dimensional
AEM	airborne electromagnetic
ALMS	airborne laser mapping system
AOL	airborne oceanographic lidar
BFGS	Broyden-Fletcher-Goldfarb-Shannon
CCRS	Canada Centre for Remote Sensing
CFT	continuous Fourier transform
CHS	Canadian Hydrographic Services
DFT	discrete Fourier transform
EMG	exponentially modified Gaussian
FIR	finite-duration impulse response
FLOPS	floating-point operations
FOV	field of view
GPS	global positioning system
HALS	hydrographic airborne laser sounder
IR	infrared
LIDAR	light detection and ranging
MPE	maximum permissible exposure

PLADS	pulsed light airborne depth sounder
PMT	photomultiplier tube
STC	sensitivity-time control
STDFT	short time Fourier transform
VLF	very low frequency

Chapter 1

Introduction

1.1 Airborne Laser Bathymetry

Airborne laser bathymetry, a state-of-the-art technology for the mapping of sea depth by using active laser ranging systems, has proved successful for charting shallow waters in many countries including Canada, Australia, and the United States. Depth information for coastal shallow waters, inland waters, and in the Arctic is of great significance to B.C. and Canada. It is essential in many areas ranging from navigation, marine charting, environmental assessment, to management of ocean resources, and for the development of ports, harbors, and marine parks. During the past fifty years, acoustic echo sounding has dominated the field of hydrography and, in particular, the field of bathymetry. Although there are new advancements in the systems used for bathymetric surveys, sonar systems require surface vessels to carry them and thus the efficiency of data acquisition is limited by the speed of the vessels. Moreover, hydrographic survey ships cannot operate safely in shallow

waters [1]. Therefore, the importance of airborne laser bathymetry should not be underestimated.

The airborne laser bathymeter LARSEN 500 developed by the Canadian Hydrographic Services (CHS) and the Canada Centre for Remote Sensing (CCRS) has been used for sea-depth estimation in shallow coastal waters by Terra Surveys Ltd., Sidney, B.C., for several years. The Hydrographic Division of the company has carried out surveys from the Canadian Arctic to South America, from Australia to Africa, and the Middle East. With the advent of laser remote sensing techniques and the demand for high resolution and accuracy in marine charts, Terra Surveys is facing major challenges in the area of bathymetry in terms of diagnosis and elimination of rogue measurements in sea-depth estimates and the enhancement, visualization, and interpretation of the results. In addition, significant improvements in the efficiency of processing the collected data is necessary especially after the new generation LARSEN 500 system, developed by Optech Ltd., North York, Ontario, is put in service. These problems are compounded by the increase in the volume of data collected by the new LARSEN 500 due to its improved resolution.

1.2 Historic Review of Bathymetry

1.2.1 Laser Bathymetry versus Acoustic Bathymetry

Remote probing of the earth's hydrosphere is severely restricted by the fact that electromagnetic radiation is strongly absorbed at all wavelengths except the very low frequency (VLF) and the blue-green portion of the optical spectrum. Although VLF signals have found a use in communications, the longer wavelengths cannot

provide the resolution required for a ranging system and it is only in the last few years that hydrographers have really begun to take advantage of the blue-green “window”. Consequently, in most underwater ranging applications, acoustic and ultra-sonic(sonar) equipment are employed.

Experiments in using sound signals to determine bathymetry began in 1915, and by the late 1920s a practical echo sounding machine had been developed by the firm Kelvin-Hughes [2]. Conventional echo sounding methods provide topographic data only along a single path directly beneath the track of survey ship [3]. Many technical refinements have occurred since then, including improved transducers to generate the sound signal and listen for its echo, and more precise timing. For shallow water bathymetry, acoustic frequencies of 20 to 200 kHz are used. For the deep oceans, lower frequencies of 2 to 20 kHz are required to obtain a strong enough echo. However, the lower the frequency, the wider the acoustic beam angle. For a simple echo sounder with a constant transducer size to have a 2° beamwidth at 10 kHz, a 3-m transducer (or array of transducers) is required, which is difficult to mechanically stabilize against roll and pitch. Two better strategies were proposed in the 1960s. These are electronically stabilized acoustic arrays and interferometry, which have more recently been adapted to multi-narrow-beam and side-scanning sonars, respectively. The side-scanning sonar method permits the measurement of the seabed topography for a wide area but the absolute depth cannot be measured. The multi-beam method has a narrower observation range but it permits measurement of the true depth. Sonar systems based on the methods mentioned above require surface vessels to carry them and thus the speed of acquisition of bathymetric data is limited by the speed of the surface vessels. Moreover, hydrographic survey ships cannot operate safely in shallow waters.

Current operational bathymetric surveys by advanced shipborne acoustic instruments provide parallel lines of depth profiles which may, or may not, be filled in with sweeps of side-scan sonar. The basic techniques remain much as they were 150 years ago but with the lead-and-line replaced by acoustic pulses. While acoustic equipment provides accurate measurement in deep waters, being shipborne it suffers from two serious limitations. The limitations are the restricted rate of coverage by the ship cruise speed and the difficulties, or even dangers, inherent in surveying unknown potentially shallow waters such as archipelagoes. In treacherous subarctic regions, bathymetry surveys for areas of special interest are not possible without an alternative remote sensing technique.

Besides the aforementioned limitations, hydrographic surveys have historically been highly capital and labour intensive, and usually take many years to complete. These logistical and economic constraints have determined the rate of data collection from bottom sounding surveys. Consequently, large areas of North American coastal and inland waters remain with either limited or outdated hydrographic data. In many areas, such as the North West and Arctic Continental shelves, there is a serious shortage of any data. Shallow water charting, in particular, is very time-consuming and expensive due to the need for additional soundings to properly delineate rocks, shoals, and other navigational hazards. These near-shore conditions frequently result in hazardous operations. Such surveys also require a large set of complementary navigational data.

Because of the expensive long-term nature of conventional shallow water charting, there is great interest in developing remote sensing methods that could complement or replace conventional methods, and could alleviate the shortage of coastal water depth information required for commercial and national defense purposes.

To this end, the application of airborne light detection and ranging (LIDAR) for bathymetry has been under very intense study for the past two decades.

The concept of making bathymetric measurements with an airborne, pulsed laser system was born in the early 60's as an offshoot of a major effort to locate submarines. Initial hydrographic requirements were based on the need for a system which could supply tactical survey data from hostile territories. The use of pulsed lasers for airborne sounding of water depth was first demonstrated in 1968 by Hickman and Hogg at the Research Centre of Syracuse University. The first experimental airborne bathymetric field trial was documented in [4]. The first commercially built system is the pulsed light airborne depth sounder (PLADS) of the U.S Naval Oceanographic Office. Notable successes were also enjoyed in Canada and Australia.

1.2.2 Development of Bathymetric Systems in Australia, Canada, and the US

The information contained in this section was compiled from literature searches. While this is not an exhaustive collection of applications and experimental work using airborne LIDAR, it should provide a general overview of how each country developed its own system. The small variations which do exist in the prospective systems, such as scanner geometry and sounding rate, are partly a consequence of the application environment. The following three subsections are devoted to the development of LIDAR systems in Australia, Canada, and the United States.

Australia

With 2.1 million km² of continental shelf, 50 percent of which is shallower than 50 m, Australia is an ideal candidate for laser bathymetry. In some instances charts in current use date back to an exploration of the coastline 180 years ago. Only

about half of the continental shelf is surveyed to acceptable standards and it was estimated recently that 49 years of work would be required to complete the job with presently available resources. It is not surprising, therefore, that the Australian system, WRELADS II, was the first laser depth sounder in the world with a verified capability to produce accurate water-depth measurements on a routine basis.

Investigations began in 1972 into the potential of airborne laser techniques as an economic means of providing speedy, large area coverage with validated depth information. Building on the experience gained in the late 1960s and early 1970s with the laser terrain profiler, WREMAPS, the Electronics Research Laboratory of the Defence Research Centre, Salisbury, developed the profiling, low repetition rate WRELADS I.

WRELADS I trials were flown in 1976-77 in South Australian gulf waters and North Queensland waters, including the Great Barrier Reef, where maximum attenuation lengths (i.e., clearest water) of 6.7 and 10 m, respectively, was observed. Water attenuation length (AL) is defined as the depth over which the laser power is attenuated by a factor of $1/e$ (≈ 0.37). Our visual range in water is generally about four ALs. Extinction depths (where the bottom signal disappears into the background noise) of 30-40 m were consistently obtained in clear waters with 15-20 m and sometimes 30 m being measured in less clear water.

After the provision of proof-of-concept and successful operation of the prototype WRELADS I system, WRELADS II was built to satisfy the requirements of the Royal Australian Navy. It scans a swath of 268 m ($\pm 15^\circ$) perpendicular to the line of flight, providing a nominal spot spacing of 10 m at 500 m altitude and an aircraft velocity of 70 m/s (cf. a shipborne echo sounder covering 10 m swath at 5 m/s).

Canada

In 1976 the Canada Centre for Remote Sensing (CCRS) tested its Mk I low-power neon laser bathymeter over Kingston Harbour in Lake Ontario and, as a result of the demonstrated success, they developed the slightly more advanced Mk II LIDAR bathymeter. This system consisted of a profiling 10 Hz Nd:YAG laser bore-sighted with stereophotography so that the LIDAR's depth accuracy complemented the ground coverage provided by photography. It was expected to have a useful depth capability of 10 m.

Surveys were conducted during 1979-80 in the St. Lawrence River, the Magdalen Islands and Bruce Peninsula in Lake Huron but the only results we have seen were for the Magdalen Islands field trials. Here the bathymeter sounded depths between 0.6 m and 20 m with an AL=1.4 m and down to 8 m in more turbid waters (AL=0.6 m).

A natural evolutionary step from the profiling Mk II was a scanning Mk III, known as LARSEN 500, which was developed by CCRS and CHS and is manufactured by Optech Ltd., North York, Ontario. The motivation for progressing to a scanning system was both for improved productivity and to enable 100 percent bottom coverage which would eliminate the risk of missing hazardous shoals.

LARSEN 500 scans in a circular fashion at 15° from nadir which is the optimum angle for minimum depth bias [5]. At an aircraft altitude of 500 m the sounder covers a swath of 350 m at 70 m/s and, through the use of a staggered-time fire control, a near uniform grid is created at a nominal spot spacing of 35 m.

United States

Research into airborne depth sounding was initiated in the United States in the late 1960s. The first commercially built research system was the pulsed light airborne depth sounder (PLADS) which was operated by the Naval Oceanographic Office of Washington, D.C. Tests on PLADS were conducted in 1972. From the bibliography, some of the NASA efforts culminated in comparison trials of two light sources: An Avco C-950 neon gas laser and a frequency-doubled Nd:YAG laser.

The following five American systems have been identified [6].

1. NASA Airborne Oceanographic LIDAR

The variable-angle conically scanning airborne oceanographic LIDAR (AOL), built by Avco Everett Research Laboratory, is based at the NASA Wallops Flight Facility and has been operating since 1977. It is capable of operating in a bathymetric mode using neon as a source (540.1 nm signal) or in a fluorescent mode using nitrogen (337.1 nm). One flight of this system off the Atlantic coast of Virginia measured to 10 m depth, while a survey of the more turbid Chesapeake Bay measured to 4.6 m. The AOL was built primarily to perform field demonstrations and technology transfer experiments for user agencies.

2. ERIM M8 active/passive scanner

This hybrid bathymetry system consists of a nitrogen-pumped pulsed dye laser (520 nm nominal output, but tunable between 360-740 nm) operated (normally at nadir) in conjunction with a nine-channel multispectral scanner. In water-depth applications, the LIDAR serves as a point calibration for an algorithm incorporating the passive data. The system has a spatial resolution of 0.61m

over a swath of 610 m and its useful water-depth capability is probably about 9-10 m.

3. Avco Airborne Laser Mapping System

The airborne laser mapping system (ALMS) uses a Nd:YAG laser at either 1064 nm for terrain mapping or 532 nm for bathymetry. The green output is capable of underwater profile measurements up to 3.3 times the measured Secchi depth described in detail in Section 1.4. This system is probably employed as a test and demonstration model since Avco is a major manufacturer of airborne lasers.

4. The DMA Hydrographic Airborne Laser Sounder

Development of the hydrographic airborne laser sounder (HALS) was initiated in 1976 by the U.S. Naval Ocean R&D activity. HALS was initially intended to be carried on an HH-2D helicopter operating from a Chauvenet class naval survey ship, but is now destined for a fixed-wing aircraft using GPS navigation. GPS positioning enables considerably greater freedom of movement in comparison to short-based transponders. HALS's purpose is to increase the amount of area surveyed annually over the United States' foreign areas of responsibility. The coverage rate is 29 km²/hour with soundings every 4-5 m and a depth capability of 28 m under typical conditions.

5. NOS Airborne Laser Hydrography System

The National Ocean Survey (NOS) has responsibility for charting the comparatively well-surveyed U.S. coastal zone. Their interest in laser hydrography is from the point of view of economy, since a laser system can survey for one-sixth

of the cost and one-fifth of the manpower of conventional launch-based sonar hydrography systems and it has been shown that a significant amount of U.S. coastal water could be surveyed by laser. The NOS system has a similar capability to HALS with $22 \text{ km}^2/\text{hour}$ coverage and soundings at 5 m intervals, but as of June 1985, no hardware development had been initiated.

1.3 Description of the LARSEN 500 Airborne Laser Bathymeter

1.3.1 The System

A typical airborne laser bathymetry system consists of a pulsed blue-green laser transmitter, a scanning mirror, a receiver telescope, a narrow-band optical filter to suppress daylight background, a photomultiplier tube (PMT) detector, signal conditioning electronics, a waveform digitizer or real-time signal processor for depth determination, and a master control computer.

The LARSEN 500 bathymeter is an active remote sensor that transmits a series of laser pulses from an aircraft at an altitude of 500 metres into the ocean and receives the reflections from the ocean surface and floor. The beams, consisting of infrared (IR) and blue-green laser pulses, scan the water surface and bottom across a swath of 270-meter with a depth penetration of up to 40 m. The blue-green transmission window of water is attractive as light in this frequency range can propagate through both air and water [7]. The laser beam geometry of the system is illustrated in Figure 1.1, and the principle of operations is as follows. The IR and blue-green laser pulses are transmitted simultaneously from the aircraft into the ocean in a quasi-circular fashion with a uniform sounding density on a grid spacing

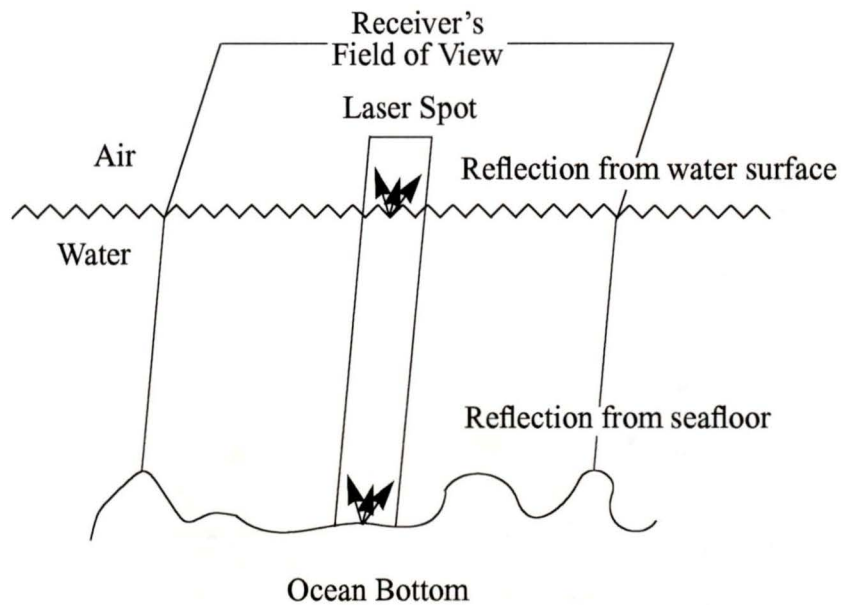


Figure 1.1: Laser beam geometry and receiver's field-of-view.

of 35 m. The system performs a circular scan across the track as it moves along the track. It is designed to produce a regular pattern of depth soundings on the surface of the sea.

1.3.2 The Signals

For each laser sounding, a waveform representing the amount of photon energy received from the reflection of the laser pulses is collected by a laser transceiver mounted on the aircraft platform. The received signal is sampled at 2-ns intervals and usually contains 256 consecutive samples. The samples are digitized to a 6-bit

accuracy representing 64 quantization levels. Depth estimation for each sounding is then carried out on the basis of the time difference between the surface and bottom reflections.

A simplified formula for estimating sea depth is given by

$$\text{depth} = \frac{T_d C}{2r} \quad (1.1)$$

where T_d is the time interval between the peaks of the blue-green surface and bottom reflections, C is the speed of light in air, and r is the refractive index of sea water. For pure water $r = 1.33$ and for oceanic water $r = 1.34$. So in water, the speed of light, C/r , is approximately equal to 0.225 m/ns. With this speed, one sample duration is equivalent to a depth of 0.225 m. This is a factor that determines the resolution of the sea-depth estimation. Various features of interest are illustrated in Figure 1.2.

1.3.3 Operational Considerations

In practice, an accurate bathymetric measurement requires that the bias caused by the effects of the geometric field of view, water clarity, and marine conditions be taken into account. Unlike acoustic signals, light is not seriously affected by temperature or salinity. The idealized geometry for timing is that a small portion of the beam is reflected from the surface while the remainder is refracted through the surface, traverses the water column along a slanted path, is then diffusely reflected by the bottom, again traverses the water column (along the same slant path), and refracts back through the surface towards the receiver. The depth is calculated by halving the round-trip time in the water and correcting for the off-nadir geometry of the scanner. The actual geometries, however, are far more complex due to physical

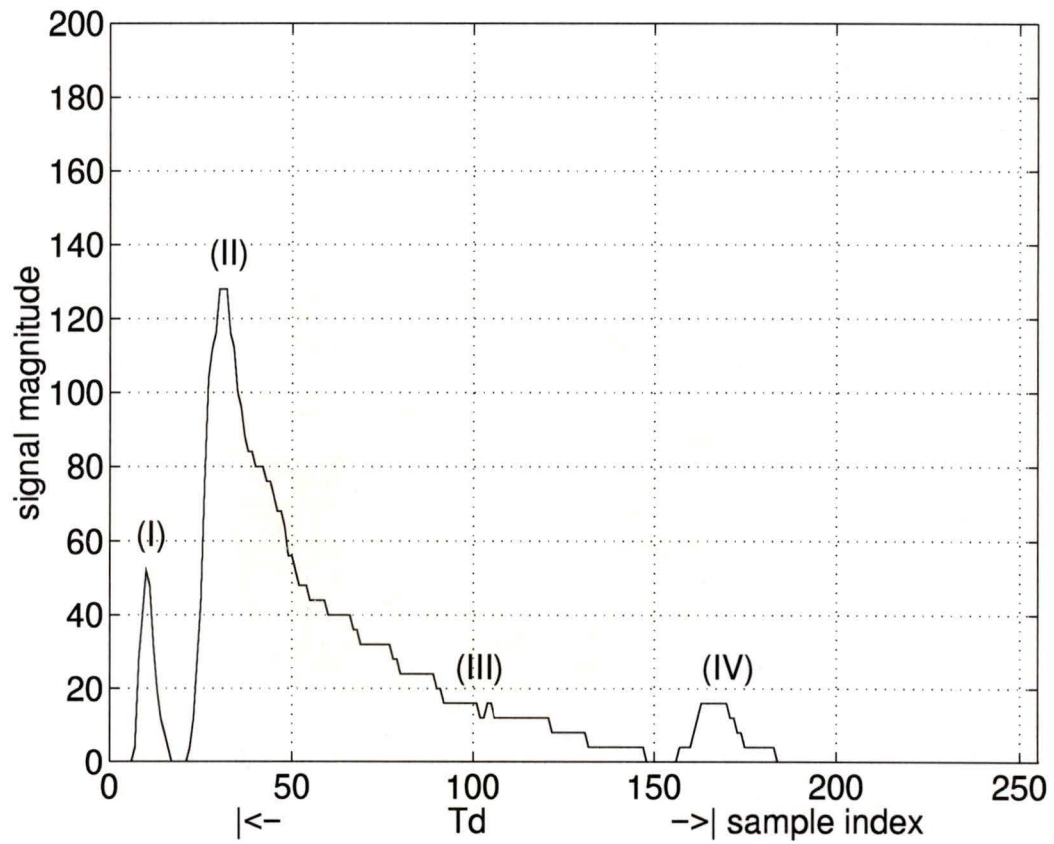


Figure 1.2: A typical bathymetric waveform. I: infrared surface reflection; II: blue-green surface reflection; III: volume backscatter; IV: bottom reflection.

interaction both at the surface and in the water column.

A LARSEN waveform represents the signature of the interactions between laser pulse signals and the air or water column. The interaction mechanisms involve reflection, scattering, absorption, refraction, emission, and so on. The major interactions that substantially influence the depth estimation and form the bulk of the signature keying are reflections from the surface and bottom of the ocean as well as backscattering from the water column along the paths that laser pulses traverse. The time difference between the return signals from the surface and bottom of the ocean plays an important role in the sea-depth estimation. The effects of backscattering from the water column occur in between the timings of these two major returns and may overlap or fuse together to some extent with the two return signals to form the received waveform. Therefore, it is important to model the backscattering signature and subtract the signature from the waveform to reduce the extent of overlap and increase the accuracy of the sea-depth estimation.

To develop the models that characterize the surface and bottom reflections as well as the backscattering envelope, a study on the signal generation process and the timing sequence of the received signals is necessary. When a laser beam hits the surface of the sea, a fraction, which is less than 5 percent of the total beam energy, is reflected back into the air and may be sensed by the receiver as a surface return signal. The magnitude of the peak surface return power depends heavily on the off-nadir beam entry angle and the wind speed [8], and can be several dozen times stronger than the weak bottom return. This extreme amplitude variation occurs within a time period of only tens to thousands of nanoseconds, and causes the leading edge of the surface return signal which usually appears with a very steep slope during the rise time. Physically at that time, the return signals of

the backscattering from the water column and bottom reflection have not yet been received. Therefore, the bulk of leading edge of the surface return can provide very accurate approximation of the return signal not only in terms of peak position but also in terms of the shape of the return signal.

1.3.4 The Laser Source

During the 60's and 70's, a variety of laser sources were developed. A few types are of special interest for practical environmental probing. They include the Nd:YAG laser, nitrogen laser, organic dye lasers, CO₂ laser and semiconductor lasers. Lasers can be classified into several categories. Very natural divisions can be made between pulsed and continuous-wave (c.w.) lasers and between fixed frequency and tunable lasers. The choice of laser clearly depends on the application. The parameters that characterize the specific laser are wavelength, linewidth, beam divergence, and output power for c.w. lasers, whereas for pulsed lasers peak power, pulse length and repetition rate are also specified. For mobile probing, such as airborne laser bathymetry, equipment weight, size, and power consumption are important parameters. In addition, reliability and price are of great practical importance. For bathymetric applications, the Nd:YAG laser is most commonly used.

The Nd:YAG laser

The Nd:YAG laser belongs to the family of solid-state lasers, the first member being the ruby laser. Lasers of this kind have as an active or amplifying medium a rod of a crystalline or glassy material. Active ions are incorporated at a low concentration in the host material. In order to achieve light amplification by stimulated emission

of radiation, population inversion must be established between two levels, connected by a suitable transition. The ions or atoms are pumped by one or several flash-lamps to achieve the inversion. Laser oscillation is accomplished by placing the amplifying medium inside a resonator consisting of two dielectrically coated mirrors, one with the highest possible reflectivity and the other semitransparent to allow part of the light to be extracted as the useful beam.

The Nd:YAG laser can be operated continuously, but the pulsed operation is more commonly used. The flash-lamps are fired with some tens of joules of electric energy, which was stored in a capacitor. The laser will quickly reach population inversion and laser action starts, with stimulated emission at $1064 \mu\text{m}$. This very quickly leads to loss of the population inversion and the laser action is terminated after the emission of a short pulse. But the flash-lamps, which are on for about $1/\mu\text{s}$, continue to pump, and a second laser flash occurs, and so on. The output of the laser will thus consist of a train of irregular laser spikes during the flash-lamp pumping. Such an output is not very useful for probing applications. However, the spiking behaviour can be prevented by blocking the light-path inside the cavity until the major part of the lamp pulse has been utilized to create a large storage of upper-state ions. This is normally done electro-optically using a Pockels cell, which switches the state of linear polarization of the transmitted light. The cavity is suddenly opened and the stored inversion is utilized for the generation of a single giant pulse. Since the Q-value of the resonator is quickly increased the technique is called Q-switching. Recently great improvements in resonator design for Nd:YAG lasers have been made allowing a very efficient extraction of the energy transferred to the laser rod.

A typical Nd:YAG laser for remote sensing applications has the following charac-

teristics: pulse energy: 100 mJ, pulse length: 10 ns, repetition rate: 10 Hz or 20 Hz, beam divergence: 1 milliradian. The peak power of the Nd:YAG laser is about 10 MW and the laser can easily be boosted by the addition of an amplifier stage. This consists of a second rod, generally of slightly larger diameter, pumped by flash-lamps in the same way as in the laser oscillator. The unit is placed outside the cavity and the maximum population inversion is established at the time when the laser pulse passes through the amplifier rod. Typical single-pulse amplification factors are 3-5. The use of an amplifier stage is frequent in remote-sensing applications.

The ruby laser is of a very similar construction. Its primary emission is at 694 nm. In addition, the doubled output at 347 nm is frequently used. The ruby laser can produce higher pulse energies but the repetition rate is normally much lower than that of the Nd:YAG laser.

1.3.5 Eye Safety

With the laser power levels used in environmental probing the beam represent a potential hazard only for a direct eye encounter. The maximum permissible exposure (MPE) of the eye limits the power used in laser remote sensing. In Table 1.1, the MPE levels for pulsed lasers given by the American National Standards Institute (ANSI) standards are shown. Three wavelength regions are treated separately here. If a further division is made, higher values can be given for some subregions. Below 400 nm (the ultraviolet region) light is absorbed by the cornea and the lens, whereas in the 400 nm - 1.4 μm region (the visible and near infrared region) the much more sensitive retina is exposed. This is the most critical region where eye safety considerations can limit the full use of the techniques. In the infrared region

Table 1.1: Maximum permissible exposure for the eye

Wavelength region	MPE J cm^{-2}
200 – 400 nm	3×10^{-3}
401 nm – 1.4 μm	5×10^{-7}
1.4 μm – 13 μm	1×10^{-2}

(> 1.4 μm) light is absorbed by the cornea, the lens, as well as by the aqueous humour. This usually results in higher allowed exposures. For a given laser, the eye safety standards can be met either directly at the system output by expanding the beam or at a certain range because of the divergence of the transmitted beam. For atmospheric probing with systems operating from the ground at a slant angle the limitations are set by possible air traffic. Downwards-looking airborne systems of course must strictly comply with regulations for the safety of ground observers.

1.3.6 System Design and Parameterization

Sounding Pattern and Flight Altitude Consideration

In order to cover a large area, the pulsed laser beam must be scanned away from the nadir to cover a swath below the aircraft. The scanner pattern on the surface is not particularly important as long as the spatial density of the pulses is moderately uniform; however, the range of the beam entry nadir angle is of major importance to the overall system performance, and it must be carefully selected. One pattern

which fulfills many requirements is the walking oval pattern. The major drawback, particularly when aircraft roll and pitch are considered, is that the range of nadir angles around a scan is larger than desirable for minimizing propagation-induced depth measurement bias errors. An ideal scanning concept is a mirror gimbaled in two axes by computer controlled servos which can utilize aircraft attitude information feedback to automatically compensate the roll and pitch and produce a truly constant scan angle.

The pulse repetition rate, $r = 2\rho H v \tan \theta$, is determined by the desired sounding density, ρ (soundings/m²), and the swath area covered per unit time, $2Hv \tan \theta$, where H is the aircraft altitude, v is the aircraft speed, and θ is the wing-to-wing nadir angle. Because the cost-benefit for the overall technique is proportional to coverage rate, a reasonably wide swath (on the order of 200 m) is desirable. Due to practical limitations, the maximum off-nadir angle is roughly 15-25 degrees (depending on the signal processing and pulse location algorithms used) and the 200-m swath width requires a minimum altitude of about 300 m. This is twice the value of 150 m at which pilots can safely fly during the daytime but about the minimum safe altitude preferred for night flights.

Optical Consideration

The laser fires narrow pulses under computer control, through optics which determine the beam divergence, to a scanner which deflects and scans the beam in the desired pattern on the water. A typical optical system concept is as follows. For two-beam systems, the beams must be collinear to avoid large depth errors due to pointing uncertainties. The use of polarization techniques depends on the desired penetration potential and the propagation-induced bias correction procedure. Po-

larizers are not beneficial for the bottom return because the added insertion loss cancels the potential benefits of improved contrast between the bottom return and the volume backscatter. Crossed polarizers can be used to reduce the magnitude of the sometimes very strong interface reflection. The reduction of the interface return is achieved at the cost of altering the backscatter information from which the scattering coefficient might be estimated. The spot size of energy arriving at the surface of the water is determined by the altitude of the aircraft and the divergence will be chosen based on wave correction and eye-safety grounds.

The departing pulse starts a slant altitude counter used for: 1) enabling the PMT and signal processor/digitizer when the pulse nears the expected water surface, 2) measuring the slant altitude of each pulse for wave correction procedures, and 3) inhibiting further pulses should the altitude be low enough to cause eye-safety violations. The counter is stopped by the receipt of the surface return. Vertical aircraft accelerations are also measured to assist in the correction process because the aircraft motion spectrum and the spectrum of observed long-period surface swell can overlap. The characteristics of the outgoing pulse such as peak power, width, etc., are monitored to ensure nominal operation.

Field-of-View, Telescope and PMT

The return waveform received from the environment is reflected by the scanner mirror into a telescope with adjustable field-of-view (FOV). The required receiver FOV will need to encompass a spot diameter equal to a significant fraction of the working depth. For a 40-m depth and a 300-m altitude, this means a full angle FOV of roughly 100 milliradians (mr). It can be seen that the power asymptotically approaches a maximum value as the FOV is increased toward the optimal value

which would have been roughly 250 mr for the case considered. An adjustable optical block in the center of the FOV might be included as a preferred alternative to polarizers to reduce the magnitude of the surface return. If used, however, the block distorts volume backscatter information, much as does polarization.

The telescope is followed by a spectral interference filter which is required for daytime operation. The bandwidth of the filter, which should be as narrow as possible given system constraints such as FOV, size, and temperature stability, will probably be on the order of 0.5-2 nm centered on the laser wavelength. Because it has an appreciable insertion loss, this filter should be bypassed or removed for nighttime operation when it is not needed.

The optical signal is converted to an electrical signal by the PMT, which is a critical component that must be selected with care. A PMT is required for optical detection because solid-state detectors currently do not have the required combination of sensitivity, gain, and noise level. The device must be fast enough so that the incoming pulse rise time will not be significantly degraded, have high quantum efficiency at the desired wavelength, and be free from anomalous high surface-signal-strength effects such as ringing or dynode afterglow which place stray signals into the waveform. The PMT should be gated so that it can be turned off when unwanted energy such as airglow from the departing pulse near the aircraft or the interface reflection is arriving and, if desired, it can be gain-controlled as a function of time. The tube should be hand-selected to have the lowest possible dark current for optimal nighttime penetration. For a collinear, two-beam system, the infrared signal would be split off by the optical system and detected separately.

Logarithmic Amplifier

A logarithmic amplifier is a prime candidate for compressing the large dynamic range which exists between relatively strong surface (or volume) returns and weak bottom returns, particularly at night when extra performance can be gained due to the much lower ambient noise level. The resulting nonlinear distortion of the waveform will cause a depth measurement bias but this is of moderate magnitude and can be compensated. The only serious alternative to a logarithmic amplifier is a PMT with a time variable gain, or so-called sensitivity-time control (STC). With STC, the PMT gain would be kept low until after the receipt of the surface return and then either quickly raised to a higher fixed level or raised exponentially as a function of time to compensate for the exponential decay of the bottom return amplitude.

Depth Calculation

One of the most important decisions in system design is the selection of either on-board or post-flight depth calculation. For the former case, the airborne signal processing hardware and software are more complex and fallible, and depth decisions are irrevocable because the waveforms are discarded. For the latter, larger volumes of recording media will be generated. Due to the numerous physical effects and error sources involved in the airborne laser bathymetry, we feel that the digitization, recording, and return of full waveforms for careful scrutiny during processing offers a significantly higher probability of accurate depth determination. Rough depth estimates can nevertheless be calculated in real time to act as a data quality indicator. Whichever solution is selected, the waveform or depth information is appropriately

tagged with ancillary information such as time, position, aircraft attitude, and system parameters and written onto magnetic media for further post-flight processing.

1.3.7 Signal Processing

The general problem of information manipulation and processing is illustrated in Figure 1.3. In the case of bathymetric signals, the interaction of laser pulses with the water and its contents is the information source, and the measurement or observation is generally the bathymetric waveform. Signal processing involves first obtaining a representation of the signal based on a signal model and then the application of some higher level transformations in order to put the signal into a more convenient form for further processing. The last step in the process is the extraction and utilization of the message information. This step may be performed either by manual pickup or automatically by algorithms. For example, a system whose function is to obtain the depth information from the bathymetric waveforms might use a spectral representation of the bathymetric signal. One possible signal transformation would be the Fourier spectra obtained over a window of the sampled data. The spectra, retaining the local characteristics of the signal, could then be used as an enhanced profile of the waveform in the subsequent depth estimation.

In general, processing of bathymetric signals can serve two purposes. First, it is a means for obtaining a general representation of the signal in either waveform or parametric form. Second, signal processing serves the function of transforming the signal representation into alternative forms which may turn out to be more appropriate to the specific applications at hand. In the rest of this thesis we will see several examples that demonstrate the importance of signal processing in the area

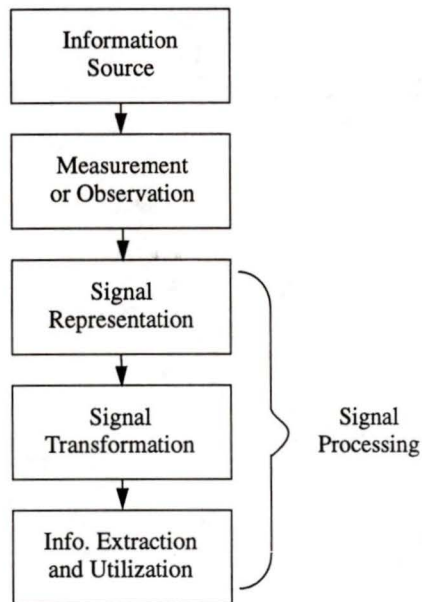


Figure 1.3: Information manipulation and processing.

of airborne laser bathymetry.

1.4 Optical Properties of Water

In this section, we present a brief description of the key optical properties and parameters of water.

1.4.1 Secchi Depth

From everyday experience, we know that as objects are lowered into the water, they become less distinct, less visible, and eventually can no longer be seen. This effect forms the basis of the first device used for measuring water clarity: the Secchi disk. The depth at which a black and white disk (roughly 18 inches in diameter) disappears from view is called the Secchi depth. Clean waters will have larger Secchi depths than dirty or more turbid waters. The disk disappears because the light traversing the water column is subject to absorption and scattering processes which reduce the magnitude of the reflected radiation and increase the volume backscatter noise background. The technique is only semi-quantitative since the results depend on a number of factors such as the angle and distribution of ambient illumination, surface wave structure, the type of particulates in the water, and the visual acuity of the observer, to name a few. The Secchi depth is consequently an apparent water property, i.e., the one which is not invariant with respect to changes in the incident radiance distribution.

1.4.2 Diffuse Attenuation Coefficient

A somewhat analogous measurement utilizing modern-day electronics involves the lowering of an appropriately filtered flat plate optical detector (photometer) through the water column to measure, as a function of depth the attenuation of incident solar irradiance, $H(\lambda)$, at wavelength λ . Irradiance is defined as the direction-cosine weighted integral of the radiance distribution over a hemispheric solid angle. The downwelling irradiance, $H(\lambda, D)$, at a depth D , decreases exponentially as

$$H(\lambda, D) = H_0(\lambda) e^{-K(\lambda)D}$$

where $K(\lambda)$ is defined as the spectral diffuse attenuation coefficient.

For monochromatic radiation, $K(\lambda)$ exhibits a strong wavelength dependence which depends on the nature of suspended materials. The attenuation minimum for this “window” in the sea varies from about 480 nm (blue) for very clear, deep, ocean water to about 570 nm (yellow-green) for highly turbid coastal water. For the moderately clear coastal waters of interest, the minimum which dictates the required laser wavelength is around 535 nm (green). This is, coincidentally, very close to the wavelength of a frequency-doubled Nd:YAG laser.

1.4.3 Beam Attenuation Coefficient

To investigate inherent optical properties, one must look directly at the scattering and absorption processes. Consider a narrow beam of collimated, monochromatic light in water with a source radiant flux N_0 , and a detector behind a pinhole at a distance d . Absorption events reduce the flux (i.e., terminate photons), and scattering events deflect photons away from the pinhole so that they do not strike the

detector. Both absorption and scattering losses behave as decreasing exponentials with increasing distance, and the radiant flux striking the detector is

$$N(\lambda) = N_0 e^{-a(\lambda)d} e^{-s(\lambda)d} = N_0 e^{-[a(\lambda)+s(\lambda)]d} \equiv N_0 e^{-\alpha(\lambda)d} \quad (1.2)$$

where $a(\lambda)$ is the absorption coefficient, $s(\lambda)$ is the scattering coefficient, and their sum, $\alpha(\lambda)$, is the beam attenuation coefficient. Note that a , s , and α are inherent parameters of the water that are spectral in character, i.e., depend on the wavelength, λ , and are expressed in units of inverse distance, m^{-1} . Henceforth, it will be understood that the optical properties are measured at the wavelength of interest, and the (λ) notation will be dropped.

The dimensionless ratio of total scattering to total attenuation, s/α , is defined as the single-scattering albedo and designated as ω_0 . Since $\alpha = a + s$, it can be seen that $0 \leq \omega_0 \leq 1$, where zero indicates pure absorption, and unity implies pure scattering. For coastal waters, ω_0 ranges roughly between 0.55 and 0.93, with 0.8 to 0.9 being typical values. It is related to the absorption-to-scattering ratio, a/s , by the expression $\omega_0 = 1/(1 + a/s)$. The greatest physical influence on ω_0 is the presence of either organic or inorganic particulates in the water column. For the studies presented here, the value of ω_0 was chosen to be 0.85. The absorption-to-scattering ratio, a/s , can be readily obtained as 0.1765. It will be shown shortly that there exists a relationship between K and α which depends almost solely on ω_0 .

1.4.4 Interrelationships of the Parameters

Due to the similarity between K (measured with some stated optical bandpass filter) and the Secchi depth, Z_s , one might expect some sort of quantitative relationship be-

tween the two measurements. Various empirical expressions of the form $KZ_s = n_K$ have been reported where $1.1 \leq n_K \leq 1.7$; however, it has been shown that n_K is not fixed but rather depends in a complex way on the scattering and absorption properties of the water and the entrained particulates, and that values of n_K outside the above range are theoretically possible. Values for K can not, therefore, be reliably inferred from Secchi disk data.

A fairly general empirical relationship has been found between α and the Secchi depth, Z_s , of the form $\alpha Z_s \approx n_\alpha$, where $6 \leq n_\alpha \leq 8$ (depending primarily on the backscatter fraction). This is somewhat surprising that α is an inherent parameter and Z_s is not, and K does not always correlate well with Z_s which shares a similar geometry. A clear linear relationship between α and $1/Z_s$ was obtained during AOL sea-truthing efforts. A value of $n_\alpha \approx 7.0$ was obtained. The Secchi depth may thus be used to estimate rough values of the beam attenuation coefficient.

1.5 Outline of the Main Results of the Thesis

This thesis contains four additional chapters and the results reported in each chapter are outlined below.

Chapter 2 presents an analysis of bathymetric signals in the time-frequency domain. The short-time discrete Fourier transform (STDFT) contains some useful information for peak identification. In particular, we show that the STDFT spectrum at $\omega = 0$ leads to improved processing results. In conjunction with a simple differentiation scheme, the STDFT of the waveform provides a new approach for depth estimation.

Chapter 3 presents the decomposition of bathymetric waveforms into three com-

ponents representing blue-green surface reflection, volume backscatter, and bottom reflection, respectively. This is followed by an introduction of a new recursive computation scheme for the three mathematical functions that are used in the waveform model. The problem at hand is then formulated as a unconstrained optimization problem. The Broyden-Fletcher-Goldfarb-Shanno (BFGS) method, which is one of the quasi-Newton methods, is employed to carry out the optimization. Simulation results on this model-based waveform characterization are presented and discussed.

Chapter 4 deals with several issues associated with the 2-D signal processing of bathymetric data. In particular, the removal of the noise that contaminates the 2-D bathymetric data is accomplished by using a two-phase approach. First, the preprocessing of depth profiles is considered. It constitutes of data segmentation, formation of a regular grid, and construction of a regularly spaced set of data by interpolation. In the second phase of the approach, an algorithm based on the use of local statistics of the depth measurements is applied to the data for the removal of noise.

Chapter 5 summarizes the results of the thesis and discusses several issues that need to be investigated in the future.

Chapter 2

One-Dimensional Processing of Bathymetric Data

In this chapter, a new one-dimensional (1-D) processing technique for estimating the sea depth from the bathymetric data is proposed. Specifically, it will be demonstrated that sea depth information, which is the main objective in the bathymetric surveys, can be obtained by the use of short-time-discrete-Fourier-transform (STDFT) method.

2.1 Bathymetric Signals

Mathematically, a bathymetric waveform is a continuous function $x_a(t)$ of time t . If $x_a(t)$ is sampled at a rate $1/T$, a corresponding discrete-time signal is obtained, which will be denoted as $x_a(nT)$, where T is the sampling period. Figure 2.1 shows an example of a bathymetric waveform represented both as an analog signal and a discrete-time signal obtained by sampling the continuous signal at a rate of 500 MHz. In subsequent figures, continuous signals are often viewed as the envelope of the corresponding sampled signals. For the sake of simplicity, the subscript of x_a will be dropped if no confusion will be caused by doing so. Also $x(nT)$ will be

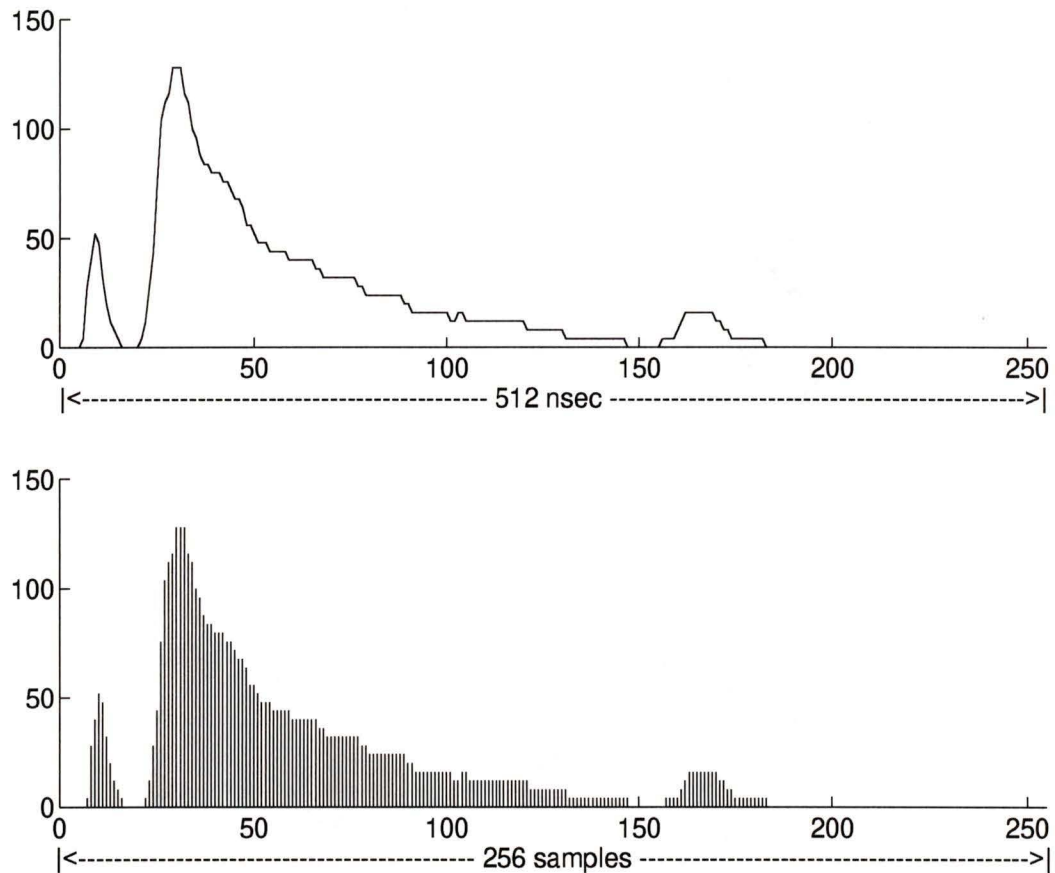


Figure 2.1: Presentation of a bathymetric signal.

replaced by $x(n)$ throughout the chapter.

2.2 The Discrete Fourier Transform

The representation of signals or other functions by sums of sinusoids or complex exponentials and the subsequent analysis on them often provide physical insight into the problem. One such representation is the discrete Fourier transform (DFT). The DFT is useful in signal processing for two basic reasons. First, it enables one to

determine the response of a linear system to an input in terms of a sum of sinusoids or complex exponentials. Second, it often serves to place in evidence certain properties of the signal that may be obscure or less evident in the original signal. Moreover, the DFT is closely related to the z transform on one hand and to the continuous Fourier transform (CFT) on the other. In fact, the DFT of a discrete-time signal is numerically equal to the discrete-frequency function obtained by sampling the z transform of the signal on the unit circle $|z| = 1$ [9].

2.2.1 The z Transform

The analysis of linear, time-invariant discrete-time systems is almost invariably carried out by using the z transform. The principal reason for this is that upon the application of the z transform, the difference equation characterizing discrete-time systems is transformed into an algebraic equation which is usually much easier to solve. The application of the z transform to a discrete-time signal $x(nT)$ yields a representation of the signal in terms of a rational function $X(z)$ where z is a complex variable. If the signal is to be processed by a discrete-time system, then the required processing can be carried out in the z domain through algebraic manipulation.

2.2.2 The Continuous-Time Fourier Transform

The continuous-time Fourier transform of a function $f(t)$ is defined by

$$F(j\omega) = \int_{-\infty}^{\infty} f(t) e^{-j\omega t} dt$$

In general, $F(j\omega)$ is complex and can be written as

$$F(j\omega) = A(\omega) e^{j\phi(\omega)}$$

where $A(\omega) = |F(j\omega)|$ and $\phi(\omega) = \angle F(j\omega)$. The functions $A(\omega)$ and $\phi(\omega)$ are called the amplitude spectrum and phase spectrum of $f(t)$, respectively.

The CFT is invertable and the function $f(t)$ can be found via the inverse Fourier transform of $F(j\omega)$ which is given by

$$f(t) = \frac{1}{2\pi} \int_{-\infty}^{\infty} F(j\omega) e^{j\omega t} d\omega$$

2.2.3 Short-time Discrete Fourier Transform

In digital-filter design and digital signal processing applications, the concept of Fourier representation has traditionally played a very important role. The standard DFT representation is appropriate for periodic, transient, or stationary random signals but may not be directly applicable for the representation of complex signals whose properties change dramatically as functions of time. Moreover, in applications where the temporal information of the original signal is manipulated during processing, a representation of the signal by the standard DFT cannot easily facilitate the processing.

In order to study the spectral properties of the aforementioned types of signals, the concept of the short-time discrete Fourier transform (STDFT) of a signal is often used. The definition and theoretical and computational details of the STDFT are considered in Section 2.3, and its application to bathymetric signals is addressed in Section 2.4.

2.3 The STDFT

2.3.1 Definitions and Properties

A spectral representation which addresses the time-varying properties of a signal is

$$X_n(e^{j\omega_k}) = \sum_{m=-\infty}^{\infty} w(n-m)x(m)e^{-j\omega_k m} \quad (2.1)$$

where $w(n-m)$ is a real window that determines the portion of the input signal that receives emphasis at a particular time index, n . The representation in (2.1) is clearly a function of two variables: the time index, n , and the frequency variable, ω_k . In other words, for each n , the window function emphasizes a number of samples of $x(n)$ and equation (2.1) returns a DFT spectrum based on the selected samples. Because of this characteristic, it is called short-time discrete Fourier transform (STDFT).

An alternative form of equation (2.1) is obtained by a change of summation index which yields the expression

$$\begin{aligned} X_n(e^{j\omega_k}) &= \sum_{m=-\infty}^{\infty} w(m)x(n-m)e^{-j\omega_k(n-m)} \\ &= e^{-j\omega_k n} \sum_{m=-\infty}^{\infty} x(n-m)w(m)e^{j\omega_k m} \end{aligned}$$

If we define

$$\tilde{X}_n(e^{j\omega_k}) = \sum_{m=-\infty}^{\infty} x(n-m)w(m)e^{j\omega_k m}$$

then $X_n(e^{j\omega_k})$ can be expressed as

$$X_n(e^{j\omega_k}) = e^{-j\omega_k n} \tilde{X}_n(e^{j\omega_k}) \quad (2.2)$$

Two interpretations may be given to equation (2.2). The first interpretation is that of a filter-bank analysis in which $X_n(e^{j\omega_k})$ is viewed as a function of n for a

fixed ω_k . In this case $X_n(e^{j\omega_k})$ can be written as the linear convolution (denoted here by $*$) of the signal $x(n)e^{-j\omega_k n}$ with the impulse response $w(n)$, i.e.,

$$X_n(e^{j\omega_k}) = [x(n)e^{-j\omega_k n}] * w(n)$$

where $w(n)$ is the impulse response function of a lowpass filter being applied to the signal $x(n)e^{-j\omega_k n}$. The modulation of $x(n)$ by $e^{-j\omega_k n}$ serves to shift the frequency spectrum of $x(n)$ at frequency ω_k to 0 frequency. Thus the STDFT can be thought of as filtering the shifted spectrum of $x(n)$ in the region of frequency ω_k by the impulse response $w(n)$.

The second interpretation of $X_n(e^{j\omega_k})$ is as the normal DFT (i.e., z transform evaluated on the unit circle) of the modified sequence

$$y_n(m) = x(m)w(n-m) \quad (2.3)$$

In this case we interpret $X_n(e^{j\omega_k})$ as a function of ω_k for a fixed value of n . Equation (2.3) shows that, for constant n , $y_n(m)$ is a product of function x and function w . Thus the normal Fourier transform of y_n is the complex convolution of the Fourier transform of x and w . As such the details of the resulting STDFT are greatly influenced by the choice of window. Thus it is important to design a window consistent with the desired time and frequency resolution of the STDFT. Throughout the chapter, we assume that the window is causal, and of duration N samples, i.e.,

$$w(n) \begin{cases} = 0, & n < 0, n > N \\ \neq 0, & 0 \leq n \leq N - 1 \end{cases}$$

For some applications such as spectrum displays, signal detection and estimation, and speech processing, the STDFT is used primarily as a nonstationary representation of the signal properties. In such cases no synthesis procedure is required.

However, for many other applications, the STDFT is used as an intermediate representation of the signal. Examples of these applications include vocoders, and signal processors where one wishes to modify the STDFT in a way that may take advantage of the nonstationary spectral properties of the signal. As such, a method for reconstructing the signal $x(n)$ from its STDFT is required. Filter-bank summation and overlap addition methods are two popular methods to synthesize a signal from the STDFT [10].

2.4 Application of the STDFT to Bathymetric Signals

Now we move on to consider applying the STDFT to bathymetric waveforms. We shall denote each of the time series waveforms collected by the laser transceiver by $x(t)$. The signal is a product of transformation of photon energy received from laser pulses reflections by the photomultiplier tube (PMT). Each signal is then sampled at 2-ns intervals and contains 256 consecutive samples. We shall denote the sampled signal as $x(n)$, where n is the sample index.

The frequency representation of the signal is denoted as $X(e^{j\omega_k})$ and is mathematically related to $x(n)$ by

$$X(e^{j\omega_k}) = \sum_{n=-\infty}^{\infty} e^{-j\omega_k n} x(n) \quad (2.4)$$

The original signal can be reconstructed from $X(e^{j\omega_k})$ by

$$x(n) = \frac{1}{2\pi} \int_{-\pi}^{\pi} X(e^{j\omega_k}) e^{j\omega_k n} d\omega_k \quad (2.5)$$

Equations (2.4) and (2.5) provide a unique correspondence between $x(n)$ and $X(e^{j\omega_k})$ and either one is an equally valid representation of the signal.

Now we analyze some typical waveforms collected by the Canadian LARSEN 500 bathymeter by using the DFT. Given the bathymetric waveform in Figure 2.2 (a), the amplitude spectrum in Figure 2.2 (b) can be obtained by applying the DFT. In Figure 2.2 (b), the horizontal axis represents the frequency span from 0 to 2π while the vertical axis represents the magnitude of the DFT of the signal. As can be easily observed, the largest frequency component of the spectrum always appears at frequency zero. As frequency ω_k increases, the magnitude of the frequency components tends to decrease. The DFT representation has several practical and conceptual limitations because it represents, for each frequency ω_k , the global (in time) characteristics of the signal. Consequently, the temporal information of the signal, which will be used for depth estimation, tends to be lost in the transform.

By using STDFT, for each different time we obtain a different spectrum and the totality of these spectra gives us a time-frequency distribution of the signal. The distribution is called spectrogram [11]. So the STDFT is a two-dimensional representation of the one-dimensional signal $x(n)$, which means that $X_n(e^{j\omega_k})$ is a function of both n , which represents time, and frequency ω_k . An example of a spectrogram of a typical waveform is shown in Figure 2.3. For a detailed look of the spectrograms at various frequencies, the four plots in Figure 2.4 are presented. It can be observed that the curve obtained by evaluating the STDFT of the signal at $\omega_k = 0$ resembles the shape of the original signal with the peaks representing the surface and bottom reflections enhanced. Consequently, the STDFT can be used for peak identification in airborne laser bathymetry. The next section will be devoted to a further discussion on the usefulness of the STDFT and the implementation issues involved.

As is stated above, the STDFT of the signal preserves the local characteristics of

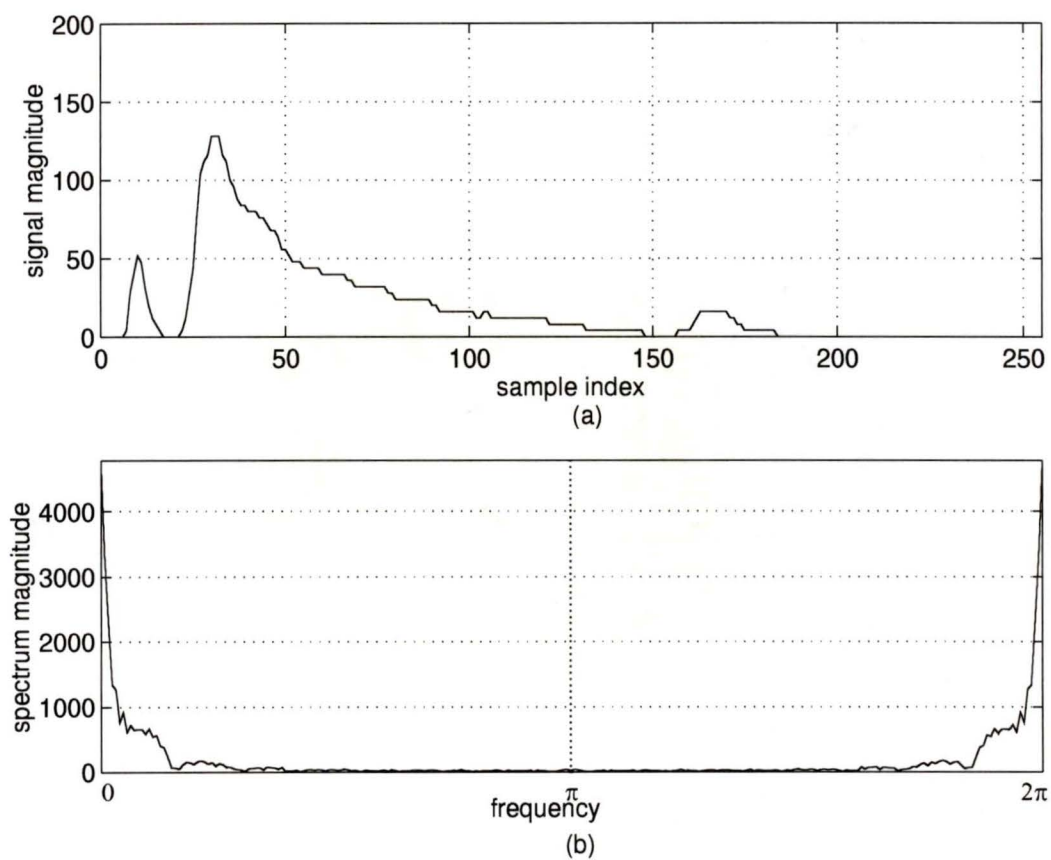


Figure 2.2: A typical waveform and its DFT spectrum (a) Original waveform (b) DFT of the waveform.

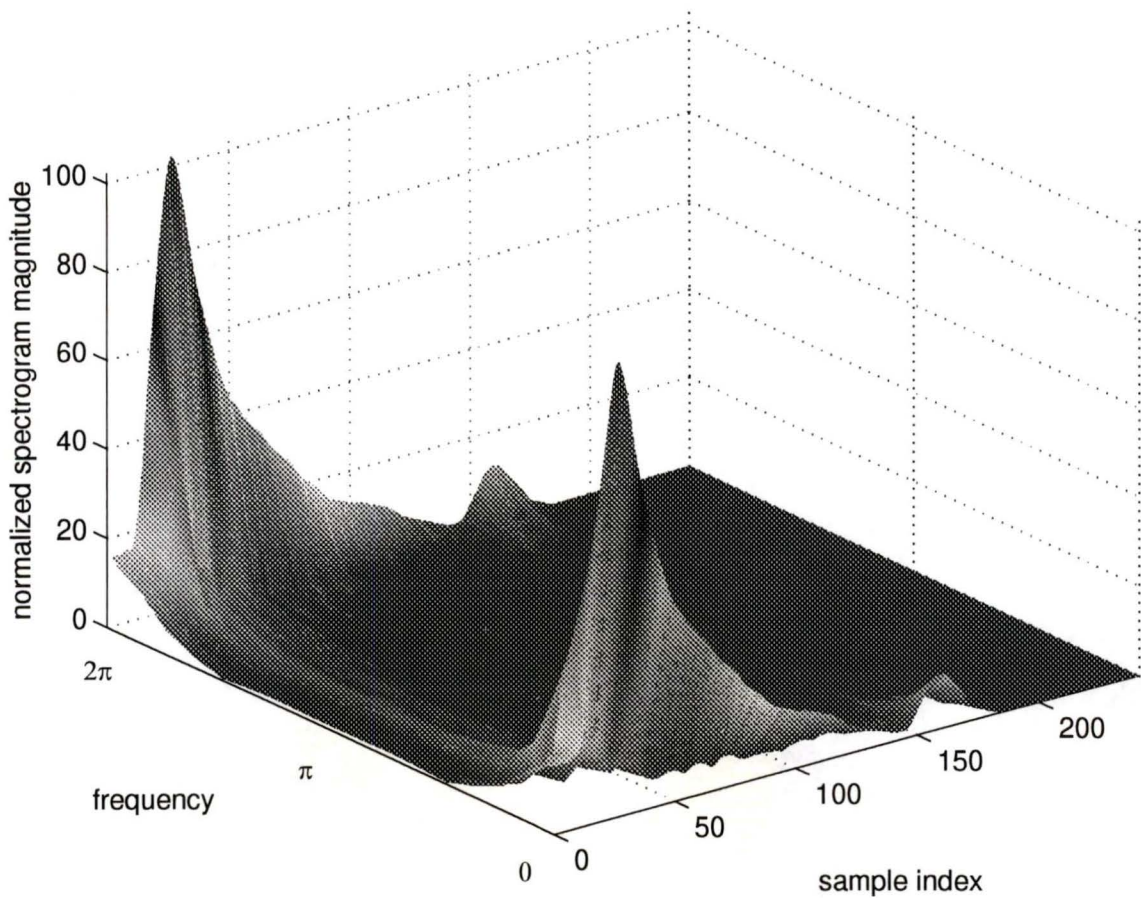


Figure 2.3: Spectrogram (normalized by the window length L) of the waveform in Figure 2.2 (a).

the signal and facilitates peak identification. The IR surface reflection, which provides timing information but does not play an important role in depth estimation, can be smoothed out in the STDFT of the original signal. This renders the processing steps simpler to carry out. Under these circumstances, we focus our attention to the STDFT spectrum at zero frequency and its evaluation.

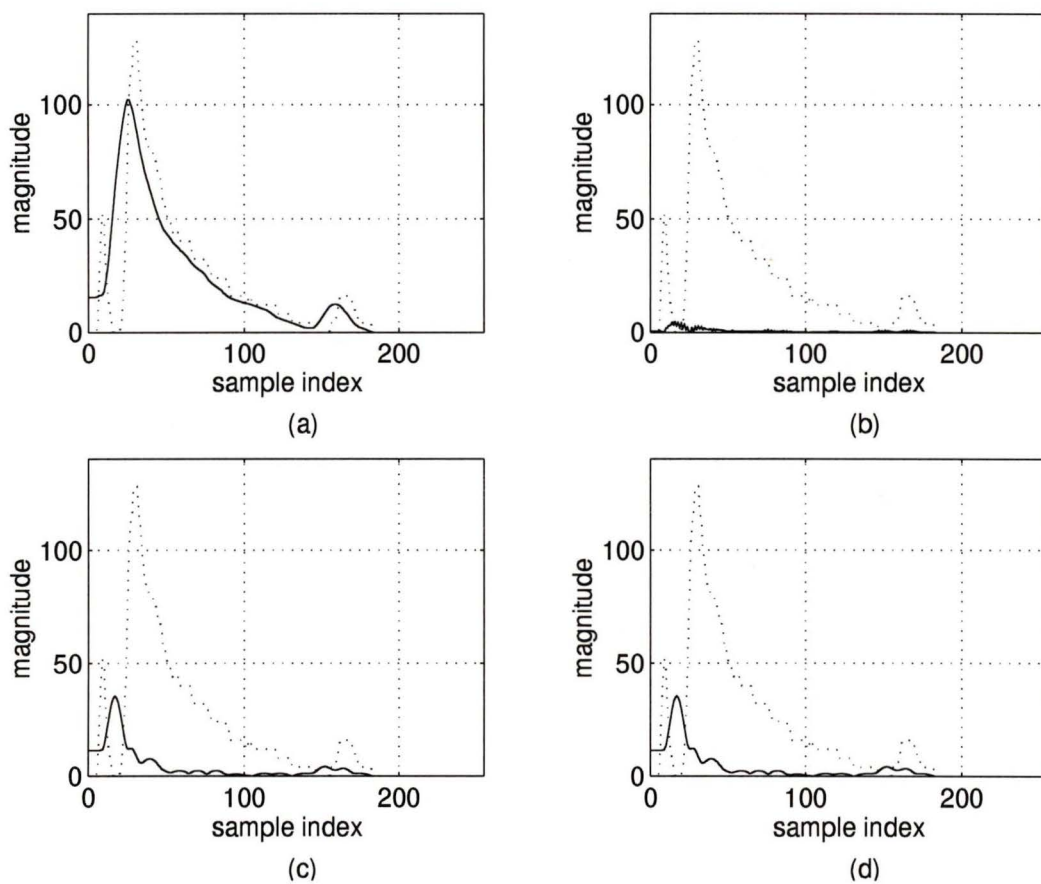


Figure 2.4: Cross-sections of the spectrogram in Figure 2.3 at some frequency components. The dotted line represents the original waveform and the solid line is the spectrogram plot. (a) $\omega_k = 0$ (b) $\omega_k = \pi$ (c) $\omega_k = \pi/(\text{window length})$ (d) $\omega_k = 2\pi - \pi/(\text{window length})$.

2.4.1 Evaluation of STDFT

From equation (2.1), the STDFT of a signal $x(n)$ is a Fourier transformation of the signal with the application of a running window, $w(n)$, defined by (2.2). As our focus is aimed on the spectrogram at zero frequency, (2.1) can be further simplified as

$$X_n = \tilde{X}_n = \sum_{m=-\infty}^{\infty} x(n-m) w(m)$$

where X_n and \tilde{X}_n denote $X(e^{j\omega_k})$ and $\tilde{X}(e^{j\omega_k})$ at $\omega_k = 0$. Since the LIDAR signals are voltage signals of nonnegative values, the magnitude of X_n grows as the window length N increases. In order to make X_n consistent with the original signal with respect to magnitude, we normalize X_n by the window length, i.e.,

$$\begin{aligned} X_n &= \frac{1}{N} \sum_{m=-\infty}^{\infty} x(n-m) w(m) \\ &= \frac{1}{N} \sum_{m=0}^{N-1} x(n-m) w(m) \end{aligned}$$

If the window function is chosen to be

$$w(n) = \begin{cases} 1, & 0 \leq n \leq N-1 \\ 0, & \text{otherwise} \end{cases}$$

then

$$\begin{aligned} X_n &= \frac{1}{N} \sum_{m=0}^{N-1} x(n-m) \\ &= \frac{1}{N} \sum_{m=1}^N x(n+1-m) \end{aligned}$$

Hence, it follows that

$$X_{n+1} = \frac{1}{N} \sum_{m=0}^{N-1} x(n+1-m)$$

$$\begin{aligned}
&= \frac{1}{N} \sum_{m=1}^N x(n+1-m) + x(n+1) - x(n+1-N) \\
&= X_n + [x(n+1) - x(n+1-N)]/N
\end{aligned}$$

From the above analysis it is quite clear that the STDFT of the signal at $\omega_k = 0$ is equal to the mean value of the signal over the window.

2.5 Peak Identification

As was mentioned earlier, the STDFT has a shape that not only preserves but also enhances the peak locations of the signal being analyzed. This renders the subsequent processing task easier to carry out. In other words, either by a simple differentiation of the STDFT or by modeling the smoothed waveform, the depth information can be easily extracted.

The rest of this chapter will discuss a technique that combines STDFT evaluation and differentiation to detect the depth information. The characterization and decomposition of waveforms using numerical optimization techniques will be the subject of discussion in the next chapter.

2.5.1 Differentiation of STDFT Spectrum

The identification of peak locations in a waveform can be done by a differentiation technique to locate the zero-crossing points of the differentiated waveform. The application of this technique to a waveform may encounter some difficulties because there exist erroneous zero-crossing points, which do not correspond to the surface and bottom reflections. A set of selection or threshold criteria for the true zero-crossing is thus required. As conditions of surveying areas change, the criteria

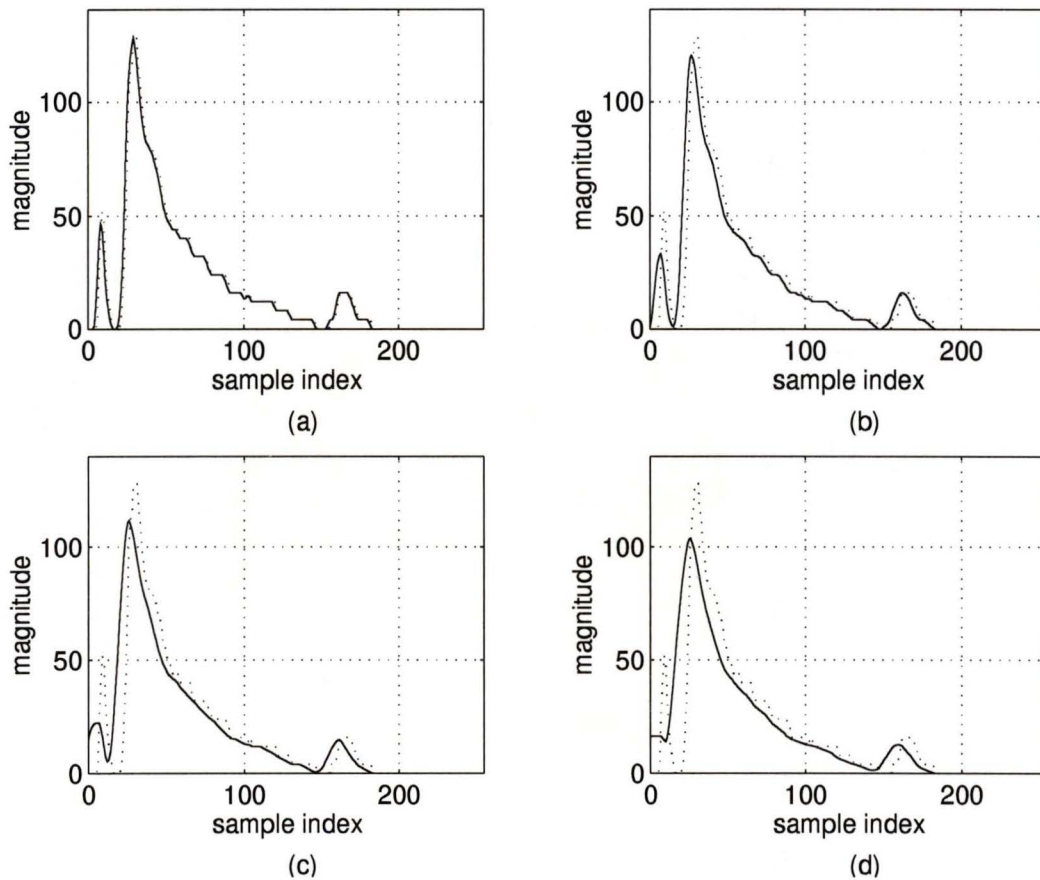


Figure 2.5: Comparison of STDFT of various window lengths with original waveform. The dotted line presents the original waveform and the solid line is the STDFT. (a) STDFT of window length 3 (b) STDFT of window length 7 (c) STDFT of window length 11 (d) STDFT of window length 15.

might be different. Therefore, this technique must be used in conjunction with certain algorithms in order to automate the selection.

As can be seen from Figure 2.5, by using a moving window of appropriate length along the time axis, the STDFT of the signal is smoothed and spurious small peaks or ringing are eliminated and the background noise is averaged out. Note that as the window length increases, the peak positions of the STDFT spectrum may shift to the left relative to the corresponding peak positions in the original waveform. However, the relative distance of the peaks between surface and bottom reflections appears to be the same in most cases, and in depth estimation what really matters is the relative distance of the peaks but not their absolute positions. Therefore, the shift effect caused by the STDFT is not a serious drawback as long as the relative distance remains within a certain tolerance while increasing the window length.

From the above observations, we note that the STDFT of a waveform at zero frequency resembles the original waveform and depth can be extracted by studying the spectrum under various window lengths. Differentiation of the STDFT at zero frequency gives the number of zero-crossing points that are either local maximum or minimum points. The true surface and bottom peaks are among the local maxima and their identification can be achieved as follows. The locations of local maxima are determined with increasing window lengths and when the number of peaks is reduced to two, these are taken to correspond to the surface and bottom reflections. For the five waveforms shown in Figure 2.6, the peak positions obtained by the method are listed column-wise in Table 2.1. As can be easily seen, the number of peaks detected decreases as the window length increases. Eventually, the two peak positions that correspond to the surface and bottom reflections are picked. The differences between the two peak positions found by the above method are very

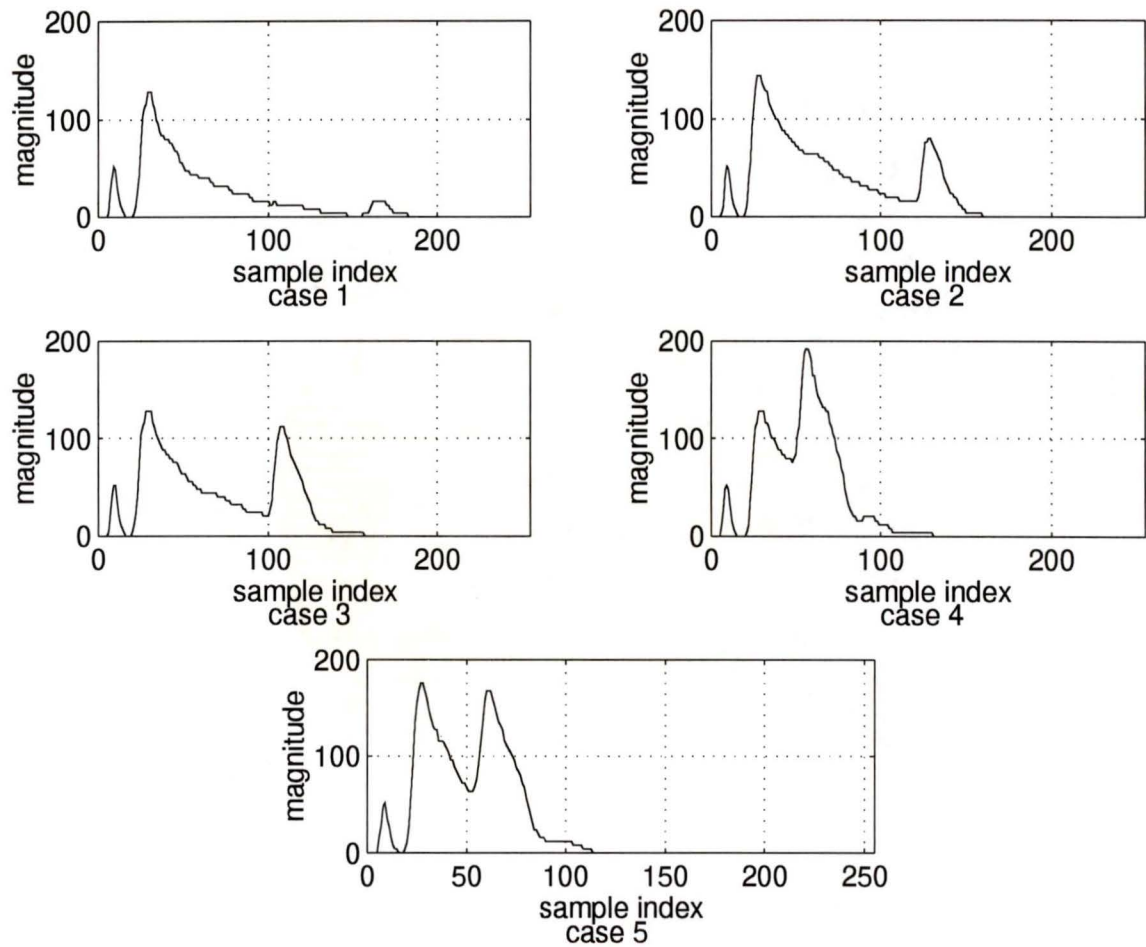


Figure 2.6: The original waveforms of the five cases used for demonstration of depth estimation by spectrogram.

similar to the differentiation method obtained by Terra Surveys.

2.6 Conclusions

The STDFT along with a differentiation technique has been applied to bathymetric data obtained by airborne laser bathymetry. The method is robust and leads to good depth estimates. The principle of the method is fairly simple and the amount of computation required is significantly less than that required by the waveform decomposition method described in the next chapter. Therefore, it is a good method for depth estimation from bathymetric waveforms.

Table 2.1: Peak Locations v.s. STDFT window length (L) (5 cases)

L	case 1	case 2	case 3	case 4	case 5
3	9 30 104 168	9 28 129	9 30 108	9 30 57 95	9 28 61
7	8 28 164	8 27 127	8 28 106	7 28 55 91	7 26 60
11	7 27 161	7 26 126	7 26 106	7 27 55	7 25 59
15	26 161	26 125	26 105	26 54	25 58
Diff	135	99	79	28	33
D_{stdft}	30.2 m	22.2 m	17.7 m	6.3 m	7.4 m
D_{ts}	30.2 m	22.1 m	17.7 m	6.4 m	7.4 m

- Diff denotes for the difference between two final peak positions in samples.
- D_{stdft} is the depth estimation from the STDFT approach.
- D_{ts} is the depth estimation from the data provided by Terra Surveys Ltd.

Chapter 3

Characterization and Decomposition of Bathymetric Waveforms

3.1 Preprocessing

In airborne laser bathymetry, the temporal position of the reflected laser pulses in the received waveforms is used to provide sea-depth information. Accurate estimation of the temporal position of these pulses is, therefore, critical. Unfortunately, there is always noise embedded in the laser waveforms that may originate from a variety of sources such as the imprecision caused by the electronic equipment of the transceiver system and the A/D quantization error resulting from the digitizing process. The aforementioned noise components may change the position of the laser pulses and, therefore, can degrade the depth-measurement accuracy. Standard lowpass filtering can remove noise in the high-frequency band but it may also deform the information content of the signal if its spectrum extends into the high-frequency band. As we have shown earlier in Chapter 2, the spectrum of bathymetric signals in general has dominant components at low frequencies and its amplitude is reduced as the

frequency increases. Therefore, a lowpass filter of appropriate order with a carefully selected 3-dB cut-off frequency can actually do the job. A finite-duration impulse response (FIR) filter of order 12 with the passband cut-off frequency being 0.0001 of the Nyquist sampling frequency was tested and found to give good results. A smoothing filter that preserves the moments of the waveforms up to a desired order was introduced in [1, 12, 13] and was implemented and tested in our simulation study. The 12th-order FIR filter of [1, 12, 13] has the impulse response

$$h(n) = \frac{1}{143} \{-11, 0, 9, 16, 21, 24, 25, 24, 21, 16, 9, 0, -11\} \quad (3.1)$$

Simulation shows that the filter reduces the noise and gives a good estimation of the waveform. After the lowpass filtering, the background noise is largely removed, and the peaks of the surface and bottom reflections remain consistent with those in the original waveform. Hence preprocessing by using an FIR lowpass filter does result in an improved waveform profile for further processing.

3.2 Characterization of Waveforms

Four features are of major importance in a bathymetric waveform, as can be seen in Figure 1.2: the surface return, the volume backscatter return, the bottom return, and background noise level. If the arrival time difference between the detected surface and bottom returns, T_d , is known, the estimated vertical water column depth can be obtained using (1.1). The magnitude of the surface return, which depends strongly on nadir angle and wind speed can be as much as several dozen times stronger than the weak bottom return. This extreme amplitude range variation occurs within a time period of only tens or hundreds of nanoseconds, which makes

it difficult to process the returning waveforms and leads to undesirable side effects such as spurious responses in the PMT and associated electronics. The shape and duration of the surface return are similar to the transmitted laser pulse, except for some stretching caused by waves. It is desirable that the transmitted pulse decay more rapidly than the volume backscatter. If this is not the case, the tail of the surface return will be the dominating signal and will greatly reduce the effective penetration. In order to assure a clean and short trailing edge, the laser must be Q-switched, and an additional cell timed to decisively terminate the pulse may be desirable. For two-color systems, the green surface return should be heavily attenuated, preferably before the PMT, in order to reduce the magnitude dynamic range in the green-light receiver.

If the time when the surface return peak occurs (measured from the time of leading edge incidence) is denoted as t_{ps} , the peak of the volume backscatter return typically occurs at a time between $2t_{ps}$ and $3t_{ps}$. The decay of the volume backscatter signal is basically exponential in time. In the absence of a surface return, the peak of the volume backscatter signal may be detected as a false surface return, and will yield a biased depth result whose magnitude depends on the pulse width and wavelength (colour). This problem must be properly handled in order to maintain the required accuracy. Decomposition of the bathymetric waveforms is therefore necessary for the estimation of the depths from the waveforms.

The combined effects of the laser reflection from the sea surface with the laser pulses backscattered from the water column are usually denoted as the surface reflection. The first component is primarily affected by the ocean surface reflectance, the field of view of the receiver, and the scan angle of the laser beam off nadir. The second component, on the other hand, depends on the optical characteristics and

depth of the sea. Since the factors that affect the reflection characteristics from the sea surface are different from those that result in the backscatter characteristics of the water column, we are motivated to characterize the two individual components separately.

For an airborne laser system, the maximum water depth from which usable bottom returns can be received is dictated by the transmitter pulse energy, the losses in the system and environment, and the dominant noise level. Extinction, i.e., loss of a usable signal, occurs as the bottom return sinks into the noise level. During daytime, the solar radiation backscattered from the water column is prohibitively strong, and a very narrow bandwidth interference filter centered on the laser wavelength is required to attenuate solar energy at all other wavelengths. Specular reflection of sunlight from the surface, namely, the glint pattern, is far too strong even with a narrow bandwidth filter, and must be carefully avoided by flying at appropriate times of day if the latitude is low enough to cause the problem. Night-time operation is preferred (but by no means required) due to the lower background noise level and, consequently, increased penetration potential.

Because of the large attenuation and spreading of the light beam in water, airborne laser bathymetry is limited to shallow waters. Maximum penetration for given water conditions and aircraft altitude are dictated by the amount of pulse energy available at a high repetition rate from state-of-the-art lasers (up to eye-safety limitations which depend on altitude and transmitter divergence). Penetration in murky harbour or bay waters may be less than 10 m. Only in moderately clean waters can day-time depths beyond 30 m be regularly accessible, and 40-50 m (depending on the bandwidth of the interference filter) is probably a practical upper limit even for extremely clean waters. There is a great deal of survey area within these depth

bounds where acoustic or sonar techniques are very slow and expensive. The prime benefits of airborne laser hydrography are the speed and economy with which these accessible shallow areas can be surveyed.

3.3 Characterization of Surface Reflection

As we can see from Figure 1.2, there are two distinct surface reflections which result from the infrared and blue-green laser pulses. The appearance of the infrared surface reflection indicates the true surface return and serves as separator of successive waveforms collected from two consecutive sounding positions. However, the infrared laser pulses of wavelength 1064 nm can only penetrate about 20 cm of the water body. On the other hand, blue-green pulses whose wavelength is about 532 nm are much less attenuated in the water and can thus serve as an effective source for penetration.

A mathematical function that can model the effect of the blue-green surface reflection is the exponentially modified Gaussian (EMG) function [12]. This function offers a variety of asymmetrical profiles that resemble the surface reflections. The function is defined by the convolution of the standard Gaussian function with an exponential decay function, i.e.,

$$\begin{aligned} Y_{EMG}(t) &= h_G S_\tau e^{-T^2/2} e^{(S_\tau - T)^2/2} \int_{S_\tau - T}^{\infty} e^{-\xi^2/2} d\xi \\ &= h_G S_\tau e^{S_\tau^2/2 - S_\tau T} \int_{-\infty}^{T - S_\tau} e^{-\xi^2/2} d\xi \end{aligned} \quad (3.2)$$

where

$$T = \frac{(t - t_G)}{\sigma_G} \quad \text{and} \quad S_\tau = \frac{\sigma_G}{\tau}$$

In (3.2) function Y_{EMG} depends on four parameters, i.e., h_G , σ_G , τ , t_G , and the asymmetry of Y_{EMG} is determined by the ratio S_τ . The peak height and peak position of Y_{EMG} , which are denoted as P and t_p , respectively, can be easily identified. From (3.2), the relationship between P and t_p can be expressed as

$$P = Y_{EMG}(t_p) = h_G S_\tau e^{S_\tau^2/2} e^{-S_\tau T_p} \int_{-\infty}^{T_p - S_\tau} e^{-\xi^2/2} d\xi$$

where t_p is the time instant at which the peak of Y_{EMG} occurs and $T_p = (t_p - t_G) / \sigma_G$. Hence

$$h_G S_\tau e^{S_\tau^2/2} = P \left[\frac{e^{(t_p - t_G)/\tau}}{I_{zp}} \right] \quad (3.3)$$

where

$$I_{zp} = \int_{-\infty}^{z_p} e^{-\xi^2/2} d\xi \quad \text{and} \quad z_p = T_p - S_\tau = \frac{(t_p - t_G)}{\sigma_G} - \frac{\sigma_G}{\tau}$$

It follows that (3.2) can be written as

$$Y_{EMG}(t) = P \left[\frac{e^{(t_p - t)/\tau}}{I_{zp}} \right] I(z) \quad (3.4)$$

where

$$z = T - S_\tau = \frac{t - t_G}{\sigma_G} - \frac{\sigma_G}{\tau} \quad \text{and} \quad I(z) = \int_{-\infty}^z e^{-\xi^2/2} d\xi$$

Integral $I(z)$ in (3.4) can be approximated by a polynomial expression [14] as

$$I(z) = \begin{cases} A(z) B(q) & \text{for } z \leq 0 \\ \sqrt{2\pi} - A(z) B(q) & \text{for } z > 0 \end{cases} \quad (3.5)$$

where

$$A(z) = e^{-z^2/2}, \quad B(q) = \sum_{i=1}^5 b_i q^i, \quad \text{and} \quad q = \frac{1}{1 + p|z|}$$

with parameters p and b_i ($i = 1, \dots, 5$) given by Table 3.1.

Table 3.1: Constants in the polynomial approximation for $I(z)$ in (3.5)

Parameter	Value
p	0.231642
b_1	0.319382
b_2	-0.356564
b_3	1.781480
b_4	-1.821260
b_5	1.330270

3.4 Characterization of Volume Backscatter

Between surface and bottom reflections, there exists a large profile that represents the laser backscatter of the water column. It is usually referred to as volume backscatter. It represents the interaction of laser pulses with the water body where suspended particles and incidental materials in the water column cause light by scattering. Throughout this study, the turbidity of the water column is assumed to be uniform. Consequently, the backscatter energy from the water column decays exponentially and causes the trailing edge of the reflection pulse to become asymmetrical. The same EMG function as in (3.2) can be used for the characterization of the backscatter. The significance of characterizing the volume backscatter in the course of sea-depth estimation is that a large amount of backscatter from the water column sometimes shifts the peak positions of the surface and bottom reflections, which may result in unreliable depth estimates.

3.5 Characterization of Bottom Reflection

The economic viability of an airborne laser bathymeter depends on the existence of large areas of relatively shallow water where satisfactory bottom returns can be detected. In the fairly flat east and Gulf coast offshore regions, a few extra meters of penetration capability can add a great deal of additional surveyable area. It is vital, therefore, that every possible effort be made during system design to maximize the penetration capability wherever practical. This is a complex task because a great many parameters affect penetration in indirect ways, and design tradeoffs must be made against other requirements. A number of such tradeoffs to meet the ultimate constraints are derived from matters of accuracy, swath width, sounding density, allowable size/weight, and state-of-the-art laser design.

The shape, duration, and magnitude of bottom returns depend in a complex way on the source pulse, the beam nadir angle, the depth of the water, the optical properties of the water, and the bottom topography. The basis for determining the fidelity of physical signals relies heavily on the performance of communication between the transmitter and receiver. In the case of airborne laser bathymetry, a pulsed laser transmitter is communicating with a colocated receiver via a complicated channel which consists of two passes through the atmosphere, two passes through the undulating air/water interface, two passes through a highly scattering and absorbing water column of variable clarity, and a bounce off a poorly reflecting bottom. Over the years, the characterization of return power has appeared in a variety of forms because the propagation of laser pulses in the water has not been well understood. Indeed, some effects can only be estimated through Monte Carlo propagation simulations.

The bottom reflection is affected by a number of factors such as sea turbidity, bottom reflectivity, sea state, and sea depth. For example, a sea bottom composed of rocks and sea grass can broaden the reflected pulse significantly while the dispersion effects of laser pulse in water may skew the bottom reflection. The Gaussian function is used to characterize the bottom reflection in the LARSEN waveform. The function is given by

$$Y_G(t) = A_{max} e^{-(t-t_{max})^2/2\sigma^2} \quad (3.6)$$

where A_{max} is the maximum amplitude of the Gaussian function, t_{max} is the instant when the maximum amplitude occurs, and σ is the standard deviation. The three parameters, A_{max} , t_{max} , σ , can be adjusted to quantify the amplitude, peak position, and width of the profile.

3.6 Recursive Computation of the Modeling Functions

In the process of characterization and decomposition of the waveforms into the three components, namely, surface reflection, volume backscatter, and bottom reflection, we need to find an optimal set of parameters for each characteristic function. This is done by using numerical optimization techniques to minimize the difference between sample values and the values calculated from the waveform model.

3.6.1 Recursive Computation of the Surface Reflection

In order to evaluate the EMG function at the sample points efficiently, a recursive computation scheme has been developed and is now described.

The EMG function at time t_k can be expressed as

$$\begin{aligned}
 Y_{EMG}(t_k) &= P \left[\frac{e^{(t_p - t_k)/\tau}}{I_{zp}} \right] I(z_k) \\
 &= Y_{EMG1}(t_k) I(z_k)
 \end{aligned} \tag{3.7}$$

where

$$z_k = \frac{t_k - t_G}{\sigma_G} - \frac{\sigma_G}{\tau}$$

$$Y_{EMG1}(t_k) = P \left[\frac{e^{(t_p - t_k)/\tau}}{I_{zp}} \right]$$

$$I(z_k) = \int_{-\infty}^{z_k} e^{-\xi^2/2} d\xi$$

At the next sampling instant $t_{k+1} = t_k + \Delta$, Y_{EMG} is given by

$$\begin{aligned}
 Y_{EMG}(t_{k+1}) &= P \left[\frac{e^{(t_p - t_{k+1})/\tau}}{I_{zp}} \right] I(z_{k+1}) \\
 &= P \left[\frac{e^{(t_p - t_k)/\tau - \Delta/\tau}}{I_{zp}} \right] I(z_{k+1}) \\
 &= Y_{EMG1}(t_k) e^{-\Delta/\tau} I(z_{k+1}) \\
 &= Y_{EMG1}(t_k) C_4 I(z_{k+1})
 \end{aligned} \tag{3.8}$$

where

$$C_4 = e^{-\Delta/\tau} \quad \text{and} \quad I(z_{k+1}) = \int_{-\infty}^{z_{k+1}} e^{-\xi^2/2} d\xi$$

We note that using (3.5) one can approximate $I(z_k)$ and $I(z_{k+1})$ by polynomials of $A(z)$ and $B(q)$ at z_k and z_{k+1} , respectively. Furthermore, $A(z_{k+1})$ can be obtained recursively through the following formulas. If we let

$$a = A(z_k) = e^{-z_k^2/2} \quad (3.9)$$

then

$$\begin{aligned} A(z_{k+1}) &= e^{-z_{k+1}^2/2} \\ &= e^{-(z_k + \Delta/\sigma_G)^2/2} \\ &= e^{-z_k^2/2} \left(e^{-\Delta/\sigma_G} \right)^{z_k} \left(e^{-\Delta/\sigma_G} \right)^{\Delta/2\sigma_G} \\ &= e^{-z_k^2/2} \left\{ \left[e^{-\Delta/\sigma_G} \right]^{z_{k-1}} \left[e^{-\Delta/\sigma_G} \right]^{\Delta/\sigma_G} \right\} \left(e^{-\Delta/\sigma_G} \right)^{\Delta/2\sigma_G} \\ &= a [C_{5,k-1} C_6] C_7 \\ &= a C_{5,k} C_7 \end{aligned} \quad (3.10)$$

where

$$C_{5,k} = C_{5,k-1} C_6 = \left(e^{-\Delta/\sigma_G} \right)^{z_{k-1}} \left(e^{-\Delta/\sigma_G} \right)^{\Delta/\sigma_G}$$

and

$$C_7 = \left(e^{-\Delta/\sigma_G} \right)^{\Delta/2\sigma_G}$$

After the function values have been obtained, we can move to the evaluation of the gradient of Y_{EMG} with respect to parameters σ_G , τ , t_G . Specifically, we have

$$\frac{\partial}{\partial \sigma_G} Y_{EMG}(t) = I(z) \frac{\partial}{\partial \sigma_G} Y_{EMG1}(t) + Y_{EMG1}(t) \frac{\partial}{\partial \sigma_G} I(z)$$

$$\begin{aligned}
 &= Y_{EMG}(t) \left\{ \frac{(t_p - t_G)/\sigma_G^2 + 1/\tau}{I_{zp}} \right\} e^{-z_p^2/2} + \\
 &Y_{EMG1I}(t) \left[(t_G - t)/\sigma_G^2 - 1/\tau \right]
 \end{aligned} \tag{3.11}$$

$$\begin{aligned}
 \frac{\partial}{\partial \tau} Y_{EMG}(t) &= I(z) \frac{\partial}{\partial \tau} Y_{EMG1}(t) + Y_{EMG1}(t) \frac{\partial}{\partial \tau} I(z) \\
 &= Y_{EMG}(t) \left[(t - t_p)/\tau^2 - \frac{\sigma_G}{\tau^2} \left(e^{-z_p^2/2}/I_{zp} \right) \right] + \\
 &Y_{EMG1I}(t) \sigma_G/\tau^2
 \end{aligned} \tag{3.12}$$

$$\begin{aligned}
 \frac{\partial}{\partial t_G} Y_{EMG}(t) &= I(z) \frac{\partial}{\partial t_G} Y_{EMG1} + Y_{EMG1}(t) \frac{\partial}{\partial t_G} I(z) \\
 &= Y_{EMG}(t) \left[- \left(e^{-z_p^2/2}/I_{zp} \right) \right] + Y_{EMG1I}(t) (-1/\sigma_G)
 \end{aligned} \tag{3.13}$$

where

$$Y_{EMG1I}(t) = Y_{EMG1}(t) e^{-z^2/2}$$

3.6.2 Recursive Computation of Bottom Reflection

The bottom return function $Y_G(t)$ can also be evaluated recursively. At time t_k , $Y_G(t_k)$ is given by

$$Y_G(t_k) = A_{max} e^{-(t_k - t_{max})^2/2\sigma^2}$$

If we let

$$b = Y_G(t_k) = A_{max} e^{-(t_k - t_{max})^2/2\sigma^2}$$

then $Y_G(t_{k+1})$ is given by

$$\begin{aligned}
Y_G(t_{k+1}) &= A_{max} e^{-(t_{k+1}-t_{max})^2/2\sigma^2} \\
&= A_{max} e^{-(t_k+\Delta-t_{max})^2/2\sigma^2} \\
&= A_{max} e^{-(t_k-t_{max})^2/2\sigma^2} e^{-\Delta^2/2\sigma^2} e^{-(t_k-t_{max})/\sigma^2} \\
&= bC_1C_{2,k}
\end{aligned} \tag{3.14}$$

where

$$\begin{aligned}
C_1 &= e^{-\Delta^2/2\sigma^2} \\
C_{2,k} &= e^{-(t_k-t_{max})/\sigma^2} \\
&= e^{-(t_{k-1}-t_{max})/\sigma^2} e^{-\Delta/\sigma^2} \\
&= C_{2,k-1}C_3 \\
C_3 &= e^{-\Delta/\sigma^2}
\end{aligned}$$

The gradient of Y_G with respect to parameters A_{max} , t_{max} , and σ can be evaluated as

$$\frac{\partial}{\partial A_{max}} Y_G(t) = Y_G/A_{max} \tag{3.15}$$

$$\frac{\partial}{\partial t_{max}} Y_G(t) = [(t-t_{max})/\sigma^2] Y_G(t) \tag{3.16}$$

$$\frac{\partial}{\partial \sigma} Y_G(t) = [(t-t_{max})^2/\sigma^3] Y_G(t) \tag{3.17}$$

3.6.3 Simulation Results

The direct and recursive computation algorithms for the evaluation of functions Y_{EMG} and Y_G were implemented using MATLAB to compare the efficiency of the

proposed scheme with direct computation. The values of parameters were chosen in the range of interest to run the MATLAB programs. The simulation results in terms of the number of floating-point operations used are given in Table 3.2. It is observed that the use of the recursive method reduces the amount of computation by 33.0% and 19.4% for the evaluation of functions Y_{EMG} and Y_G , respectively.

Table 3.2: Computation complexity: recursive versus direct

Function Name	Direct (FLOPS)	Recursive (FLOPS)	Reduction in percentage
Y_{EMG}	10220	6850	34.0 %
Y_G	1283	1035	19.4 %

3.7 Optimization

As was mentioned earlier, the waveform can be modeled mathematically as

$$Y_T(t) = Y_{EMG}(t) + Y_G(t) + Y_{BS}(t) \quad (3.18)$$

where $Y_T(t)$ is the lowpass-filtered waveform, $Y_{EMG}(t)$ is the surface reflection function, $Y_G(t)$ is the bottom return function, and $Y_{BS}(t)$ is the laser pulse backscatter from the water column. In order to determine the parameters of these functions, we define the objective function

$$E(\mathbf{x}) = \sum_{k=1}^m e_k^2(\mathbf{x}) = \mathbf{e}(\mathbf{x})^T \mathbf{e}(\mathbf{x}) \quad (3.19)$$

where

$$\begin{aligned} \mathbf{e}(\mathbf{x}) &= [e_1(\mathbf{x}) \cdots e_k(\mathbf{x}) \cdots e_m(\mathbf{x})]^T \\ e_k(\mathbf{x}) &= e(\mathbf{x}, t_k) = Y_T(t) - y(t_k) \\ \mathbf{x} &= [x_1 \cdots x_i \cdots x_n] \end{aligned}$$

The gradient of the objective function in (3.19) can be expressed as

$$\mathbf{g}(\mathbf{x}) = 2\mathbf{J}^T(\mathbf{x}) \mathbf{e}(\mathbf{x}) \tag{3.20}$$

where

$$\mathbf{J}(\mathbf{x}) = \begin{bmatrix} \frac{\partial e_1}{\partial x_1} & \cdots & \frac{\partial e_1}{\partial x_i} & \cdots & \frac{\partial e_1}{\partial x_n} \\ \vdots & & \vdots & & \vdots \\ \frac{\partial e_k}{\partial x_1} & \cdots & \frac{\partial e_k}{\partial x_i} & \cdots & \frac{\partial e_k}{\partial x_n} \\ \vdots & & \vdots & & \vdots \\ \frac{\partial e_m}{\partial x_1} & \cdots & \frac{\partial e_m}{\partial x_i} & \cdots & \frac{\partial e_m}{\partial x_n} \end{bmatrix}$$

t_k is the value of t at the k th sample, $y(t_k)$ represents the value of the waveform at t_k , and $Y_T(t_k)$ is defined by (3.18) using optimization, $E(\mathbf{x})$ can be minimized with respect to parameters \mathbf{x} [1, 12, 13].

3.7.1 The BFGS Optimization Method

Several quasi-Newton methods are available [15, 16]. The Broyden-Fletcher-Goldfarb-Shanno (BFGS) method is one of the robust and efficient quasi-Newton methods, and it was found to give good results in the above minimization. At each iteration, the BFGS algorithm determines the search direction vector $\mathbf{d}_k = -\mathbf{S}_k \mathbf{g}_k$ by

updating the $n \times n$ matrix \mathbf{S}_k using the formula

$$\mathbf{S}_{k+1} = \mathbf{S}_k + \left(1 + \frac{\boldsymbol{\gamma}_k^T \mathbf{S}_k \boldsymbol{\gamma}_k}{\boldsymbol{\gamma}_k^T \boldsymbol{\delta}_k}\right) \frac{\boldsymbol{\delta}_k \boldsymbol{\delta}_k^T}{\boldsymbol{\gamma}_k^T \boldsymbol{\delta}_k} - \frac{(\boldsymbol{\delta}_k \boldsymbol{\gamma}_k^T \mathbf{S}_k + \mathbf{S}_k \boldsymbol{\gamma}_k \boldsymbol{\delta}_k^T)}{\boldsymbol{\gamma}_k^T \boldsymbol{\delta}_k} \quad (3.21)$$

It can be shown [15] that if matrix \mathbf{S}_k is positive definite, then \mathbf{S}_{k+1} obtained from (3.21) is also positive definite, hence $\mathbf{d}_{k+1} = -\mathbf{S}_{k+1} \mathbf{g}_{k+1}$ is a descent direction. Moreover, the BFGS method converges to a local minimum of the objective function with a rate comparable to that of the Newton method without evaluating the Hessian matrix.

The first block of 35 samples is largely contributed by the surface reflection, since the backscatter envelop and bottom return are negligible in this range. Thus $Y_T(t)$ in (3.18) can be simplified as

$$Y_T(t) = Y_{EMG}(t) \quad (3.22)$$

By applying BFGS optimization to the objective function defined by (3.19) with $Y_T(t)$ given by (3.22), we can determine the values of the parameters of $Y_{EMG}(t)$. Having done this, we subtract the modeled surface return signals, i.e., $Y_{EMG}(t)$ from the smooth waveform data, which is obtained by applying a 12th-order lowpass filter [9] to the original waveform. Next the resulting waveform is processed by a similar procedure for subtraction of the effect of volume backscatter. Finally, we proceed to identify the bottom reflection by applying the BFGS method to the objective function in (3.19) with

$$Y_T(t) = Y_G(t) \quad (3.23)$$

to determine the values of the parameters for $Y_G(t)$. The depth can be readily estimated using the parameters obtained.

3.8 Simulation Results

The above decomposition scheme in conjunction with BFGS optimization was applied to 8 diverse bathymetric waveforms, and the results obtained are shown in Figures 3.1-3.4. As can be seen in Figures 3.1-3.4, the waveform profiles are decomposed into three components, and the depth estimates are obtained by evaluating the time difference between the surface and bottom reflections. As we can see from Table 3.3 the depth tends to be larger than the depth estimation of Terra Surveys. This problem was also encountered by other researchers. It can be solved by introducing a bias deduction scheme. The possible subtraction can be a depth dependent scheme ranging from 0.22 m to 0.44m according to the depth range. If the depth is greater than 10 m, use 0.22 m to deduce the depth, otherwise use 0.44 m. (0.22 m is equivalent to one sampling interval in the time axis). On the other hand, the depth estimation algorithm proposed in Chapter 2 in general produces a lower depth than the depth estimation of Terra Surveys and tends to be larger for depths range from 25 m to 35 m.

Since the waveform decomposition involves an optimization method that minimizes the sum of three characteristic functions for surface, volume backscatter, and bottom reflections, the number of iterations and floating-point operation (FLOPS) shown in Table 3.3 can only serve as a rough indication of the computation complexity of the algorithm.

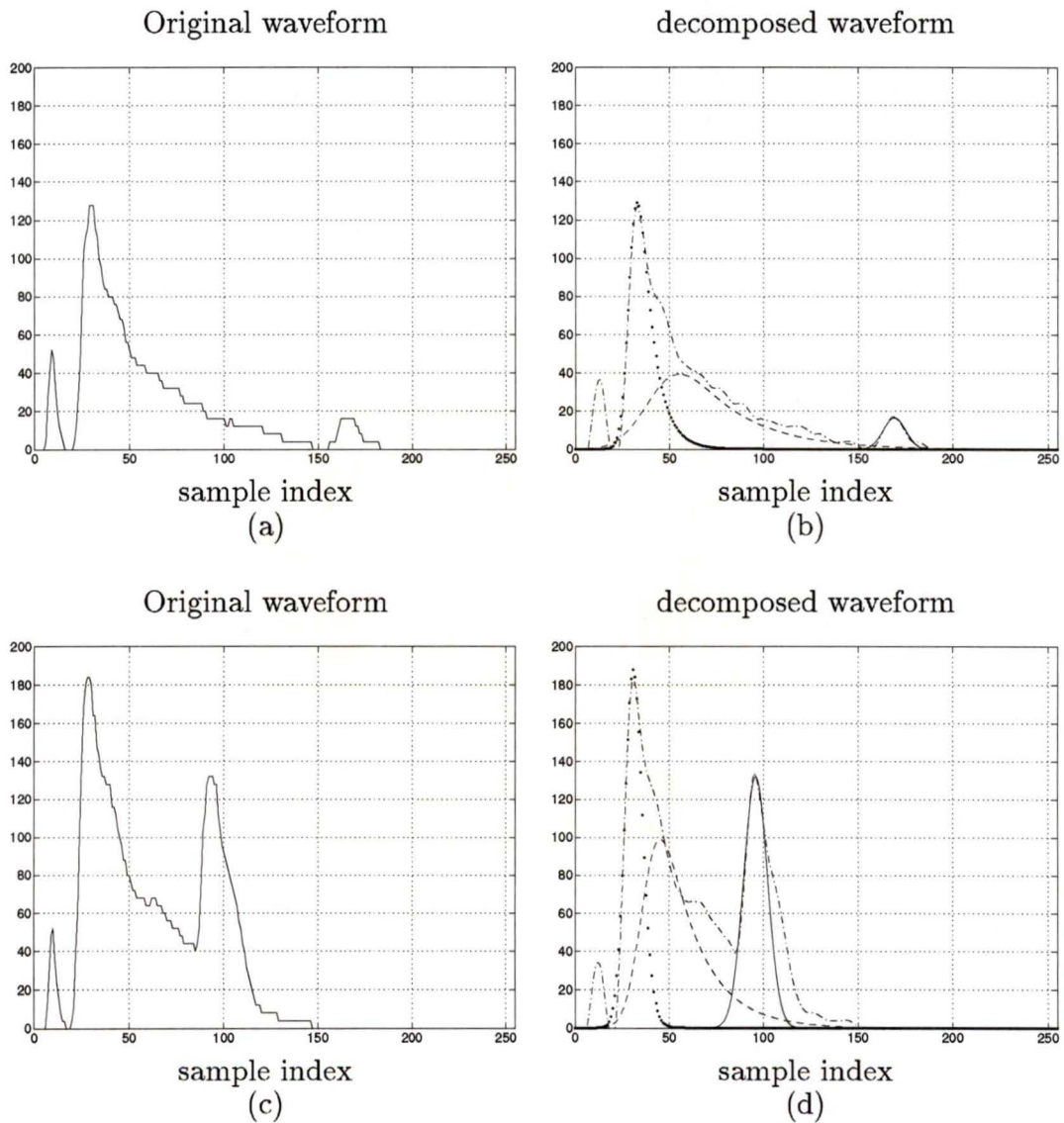


Figure 3.1: Waveform decomposition of bathymetric data. (a) and (c) Actual bathymetric waveforms, (b) and (d) the dotted line is the blue-green surface reflection, the dashed line is volume backscatter, the solid line is bottom reflection, and the dashdot line is the smoothed waveform using a 12th-order FIR filter.

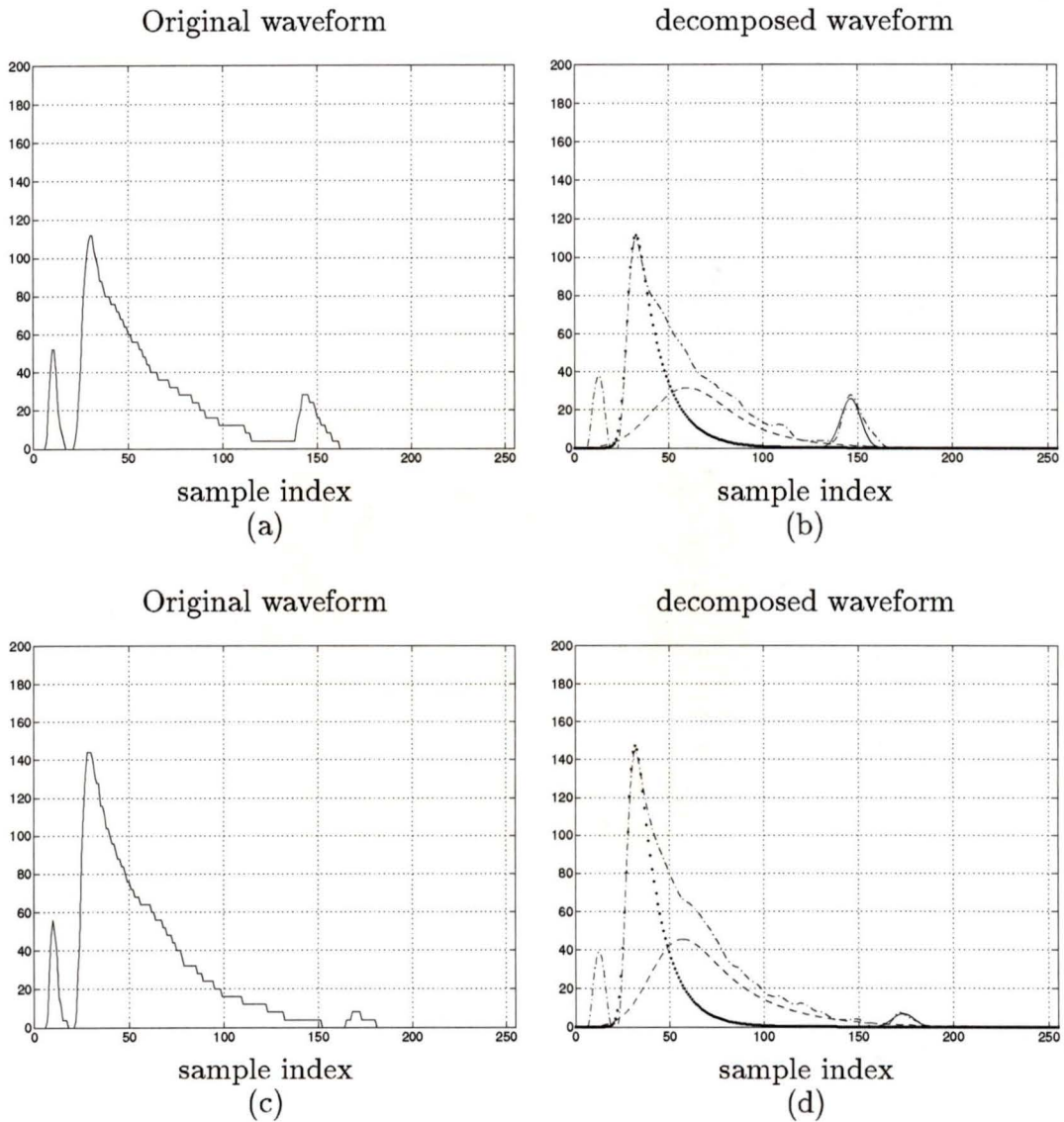


Figure 3.2: Waveform decomposition of bathymetric data. (a) and (c) Actual bathymetric waveforms, (b) and (d) the dotted line is the blue-green surface reflection, the dashed line is volume backscatter, the solid line is bottom reflection, and the dashdot line is the smoothed waveform using a 12th-order FIR filter.

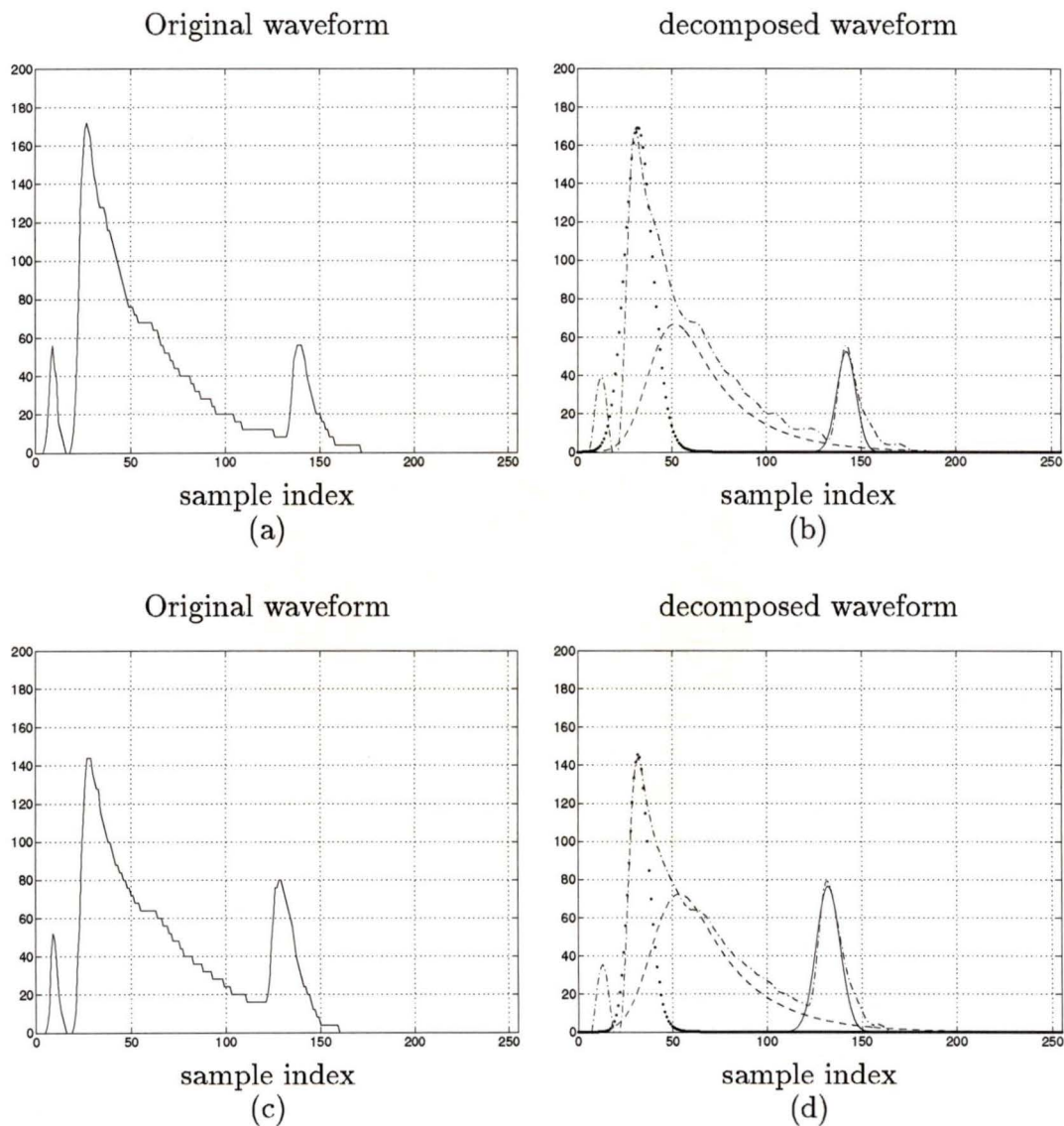


Figure 3.3: Waveform decomposition of bathymetric data. (a) and (c) Actual bathymetric waveforms, (b) and (d) the dotted line is the blue-green surface reflection, the dashed line is volume backscatter, the solid line is bottom reflection, and the dashdot line is the smoothed waveform using a 12th-order FIR filter.

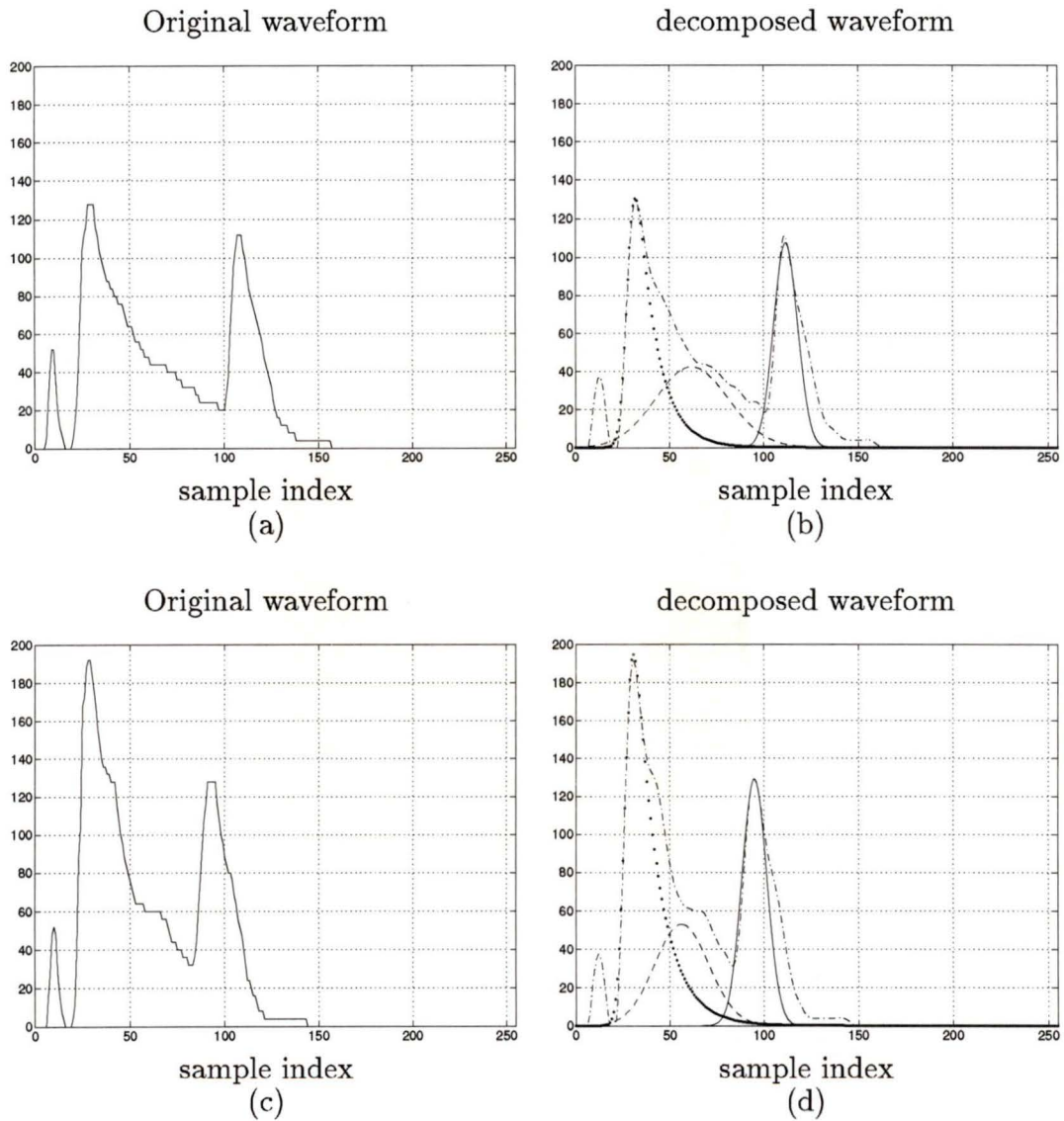


Figure 3.4: Waveform decomposition of bathymetric data. (a) and (c) Actual bathymetric waveforms, (b) and (d) the dotted line is the blue-green surface reflection, the dashed line is volume backscatter, the solid line is bottom reflection, and the dashdot line is the smoothed waveform using a 12th-order FIR filter.

Table 3.3: Simulation results of several waveforms by waveform decomposition

Figure	Surface component X_1^* , iter. #	Backscatter component X_2^* , iter. #	Bottom component X_3^* , iter. #	Total FLOPS M	Depth of decomp. D_{wd} , m	Depth of Terra Surveys D_{ts} , m
3.1 (a)	23	4	7	1249845	30.4	30.2
3.1 (c)	10	6	6	818102	14.5	14.2
3.2 (a)	30	6	7	2078020	25.3	25.2
3.2 (c)	30	5	4	1959716	31.6	31.1
3.3 (a)	2	5	7	1202748	24.6	24.5
3.3 (c)	4	5	6	739279	22.4	22.1
3.4 (a)	35	14	6	3793731	17.9	17.7
3.4 (c)	34	16	5	3998326	14.3	14.2

3.9 Conclusions

A new parametric model which consists of three signal components characterizing the surface reflection, volume backscatter, and bottom reflection has been proposed. It has been shown that the functions involved in the model can be evaluated by using recursive formulas.

On comparing the proposed algorithm with an existing evaluation method which computes the function values directly [13], our algorithm yields a 30 percent reduction in the number of FLOPS. The values of the model parameters are obtained by applying an optimization method to a least-squares objective function. Simulations have been included to illustrate the methods proposed.

In Chapters 2 and 3, we introduced two different approaches to estimate ocean depths. In Chapter 2, the STDFT of bathymetric signals at zero frequency are first evaluated. By increasing the size of the window function, depth estimation is readily obtained through differentiation of the spectrum with the sequence of variable window-size function. In Chapter 3, depth estimation is through characterization and decomposition of the waveform with the recursive evaluation of the parametric functions.

For the purpose of depth information extraction, the STDFT of the waveform signals appears to be the preferable method because of its less complexity in computation. However, the information provided by the decomposition method may be useful in marine engineering research, for example, for the measurement of turbidity.

Chapter 4

Two-Dimensional Processing of Bathymetric Topography

4.1 Introduction

In airborne laser bathymetry, noise embedded in sea-depth estimates can be broadly divided into two types. The first type of noise is in the form of background noise and quantization error. This type of noise can be removed by using the 1-D signal processing techniques described in [1, 17]. The second type is noise inherent in the 2-D bathymetric profiles that is difficult to detect in individual waveforms and is, therefore, difficult to eliminate with 1-D signal processing techniques. This type of noise generally depends on the positioning of laser soundings, sea state during the survey mission, and the measurement errors of the LIDAR system. Specifically, the geographical position of each laser sounding is dependent on the laser-firing angle, aircraft position, and altitude information. In addition, transient influences such as fish shoals or floating vegetation cause incorrect reflection timing by false returns that cannot be identified by 1-D processing of a single sounding waveform. Measurement inaccuracies due to one or more of these factors contribute uncertainties

in the laser-sounding location and, in turn, give rise to uncertainties in the depth estimates at the recorded geographical positions. Solving these problems require 2-D signal processing [18].

4.2 Preprocessing

The depth estimated by using the algorithms developed in Chapters 2 and 3 can be viewed as a function of position coordinates, i.e.,

$$\text{Depth} = F(X, Y) \quad (4.1)$$

where X is the northing coordinate and Y the easting coordinate. A graphical representation of the depth function is usually desired to visualize the trend and variations of the ocean topography of the area surveyed. We can learn from Figure 4.1 that the laser soundings provided by the airborne laser bathymetry system discussed in this thesis are distributed irregularly in a rectangular coordinate system, which may cause difficulty for some signal-processing algorithms. In what follows, we shall describe two issues that need to be considered before applying 2-D filtering for noise removal. These are data segmentation of the input data and an interpolation method to obtain regularly spaced data from irregularly spaced data.

4.2.1 Data Segmentation

A survey area usually consists of thousands of soundings. In some cases, depth information is not available in the waveform received either because laser pulses from the bathymetric sensor hit a small island, in which case there is no depth to measure, or because the surveying area is too deep, too turbid, or full of ocean

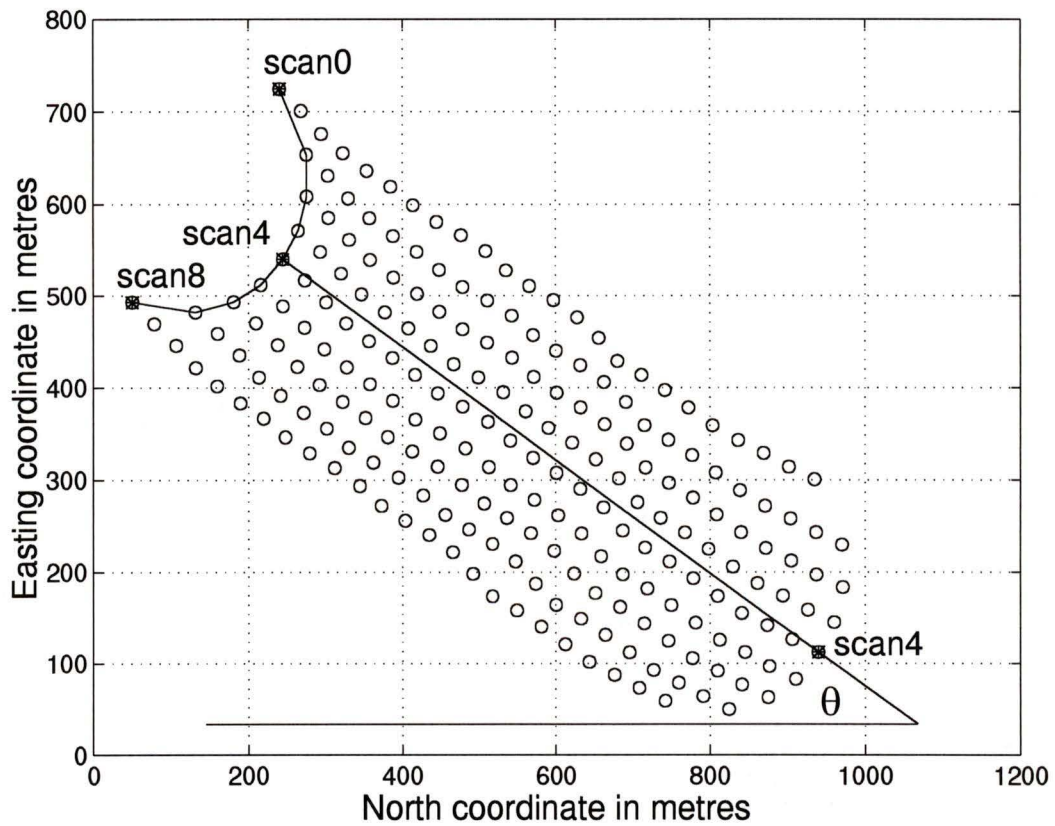


Figure 4.1: Scattering sounding pattern.

vegetation, in which case the depth is not detectable. So, before the application of 2-D filtering, it is always desirable that useless soundings be eliminated and the data size for the 2-D signal processing be sufficiently large so that soundings at the boundary represent only a small portion of the total number of soundings being processed. This part of processing is referred to as data segmentation. The heading information such as the event number, scan number, and the coordinates of northing and easting for each waveform signal as well as the estimated depth can be used to facilitate the implementation of the data segmentation and the data interpolation discussed in the next subsection. What follows is devoted to a brief description of the heading elements that are used for data segmentation and data interpolation. An integer event number is assigned to each and every waveform recorded at a survey area. The number is serial and stands for the sequence of the waveforms being collected. For the nine soundings in each arc, a scan number ranging from 0 to 8 is given to every waveform in the arc according to the order of the laser pulse sounding. A single waveform $x(n)$ is labeled as $x_{b_i}^{a_i}(n)$ to include information of the scan number, recorded as superscript a_i , and the event number, recorded as subscript b_i .

4.2.2 Data Interpolation

As mentioned above, the positions of the soundings usually exhibit an irregular pattern in a rectangular global positioning system (GPS). In addition, the boundary of a data segment is often not in parallel to the X or Y directions of the coordinate system. A regularization of scattered data is first formed as shown in Figure 4.2. Data with respect to a regular grid pattern can be obtained by the simple interpolation

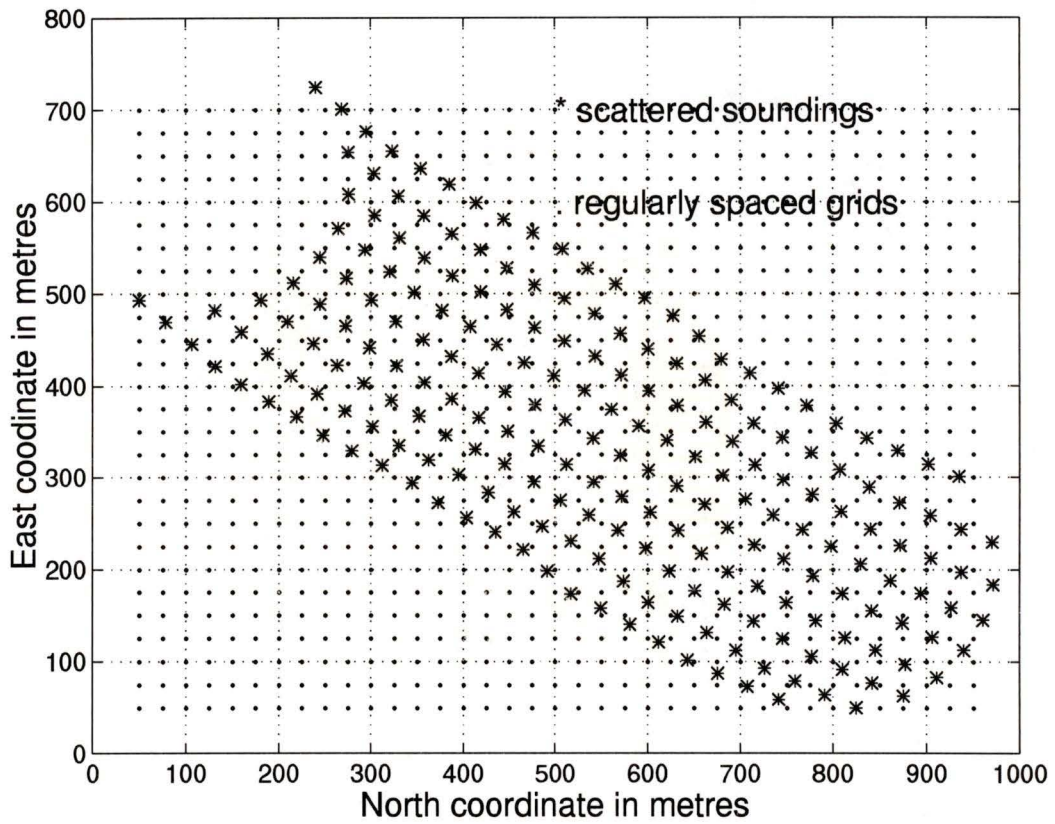


Figure 4.2: Formation of regularly spaced data.

described below. Assuming that the X and Y coordinates of a grid point are given, the depth at the point can be interpolated from the depths at four other irregularly spaced points in the vicinity of the grid point by the use of a second-order bivariate polynomial. A polynomial in six terms, which comprises a constant term, two linear terms (x , y), two quadratic terms (x^2 , y^2), and a cross-product term (xy), is used to approximate the depth data. A set of four linear equations, formed by polynomial fitting, is rearranged in matrix form.

The X and Y coordinates and the depths at the four points are $X(b_i)$, $Y(b_i)$, and $F(X(b_i), Y(b_i))$, where $i = 1, \dots, 4$. The X and Y coordinates and the depths at the grid point of interest are denoted as $X(b^*)$, $Y(b^*)$, and $F(X(b^*), Y(b^*))$. We can write

$$F(X(b_i), Y(b_i)) = a_0 + a_1 d_{x_i} + a_2 d_{y_i} + a_3 d_{x_i}^2 + a_4 d_{y_i}^2 + a_5 d_{x_i y_i} \quad (4.2)$$

where

$$\begin{aligned} d_{x_i} &= X(b^*) - X(b_i) \\ d_{y_i} &= Y(b^*) - Y(b_i) \\ d_{x_i y_i} &= d_{x_i} \cdot d_{y_i} \end{aligned}$$

Equation (4.2) can be further rearranged in matrix form as

$$F(X(b_i), Y(b_i)) = \mathbf{D}_i \mathbf{A} \quad (4.3)$$

where

$$\begin{aligned} \mathbf{D}_i &= [1 \ d_{x_i} \ d_{y_i} \ d_{x_i}^2 \ d_{y_i}^2 \ d_{x_i y_i}] \\ \mathbf{A} &= [a_0 \ a_1 \ a_2 \ a_3 \ a_4 \ a_5]^T \end{aligned}$$

for $i = 1, \dots, 4$. The four equations of (4.3) can be rearranged as

$$\begin{bmatrix} F(X(b_1), Y(b_1)) \\ F(X(b_2), Y(b_2)) \\ F(X(b_3), Y(b_3)) \\ F(X(b_4), Y(b_4)) \end{bmatrix} = \begin{bmatrix} 1 & d_{x_1} & d_{y_1} & d_{x_1}^2 & d_{y_1}^2 & d_{x_1 y_1} \\ 1 & d_{x_2} & d_{y_2} & d_{x_2}^2 & d_{y_2}^2 & d_{x_2 y_2} \\ 1 & d_{x_3} & d_{y_3} & d_{x_3}^2 & d_{y_3}^2 & d_{x_3 y_3} \\ 1 & d_{x_4} & d_{y_4} & d_{x_4}^2 & d_{y_4}^2 & d_{x_4 y_4} \end{bmatrix} \mathbf{A}$$

or

$$\mathcal{F} = \mathcal{D} \cdot \mathbf{A} \quad (4.4)$$

where

$$\mathcal{F} = \begin{bmatrix} F(X(b_1), Y(b_1)) \\ F(X(b_2), Y(b_2)) \\ F(X(b_3), Y(b_3)) \\ F(X(b_4), Y(b_4)) \end{bmatrix}$$

$$\mathcal{D} = \begin{bmatrix} 1 & d_{x_1} & d_{y_1} & d_{x_1}^2 & d_{y_1}^2 & d_{x_1 y_1} \\ 1 & d_{x_2} & d_{y_2} & d_{x_2}^2 & d_{y_2}^2 & d_{x_2 y_2} \\ 1 & d_{x_3} & d_{y_3} & d_{x_3}^2 & d_{y_3}^2 & d_{x_3 y_3} \\ 1 & d_{x_4} & d_{y_4} & d_{x_4}^2 & d_{y_4}^2 & d_{x_4 y_4} \end{bmatrix} = \begin{bmatrix} \mathbf{D}_1 \\ \mathbf{D}_2 \\ \mathbf{D}_3 \\ \mathbf{D}_4 \end{bmatrix}$$

A solution of the above set of linear equations is then obtained by applying a pseudoinverse matrix operation on the nonsquare coefficient matrix \mathcal{D} [19]. We can write

$$\mathbf{A} = \mathcal{D}^+ \mathcal{F} \quad (4.5)$$

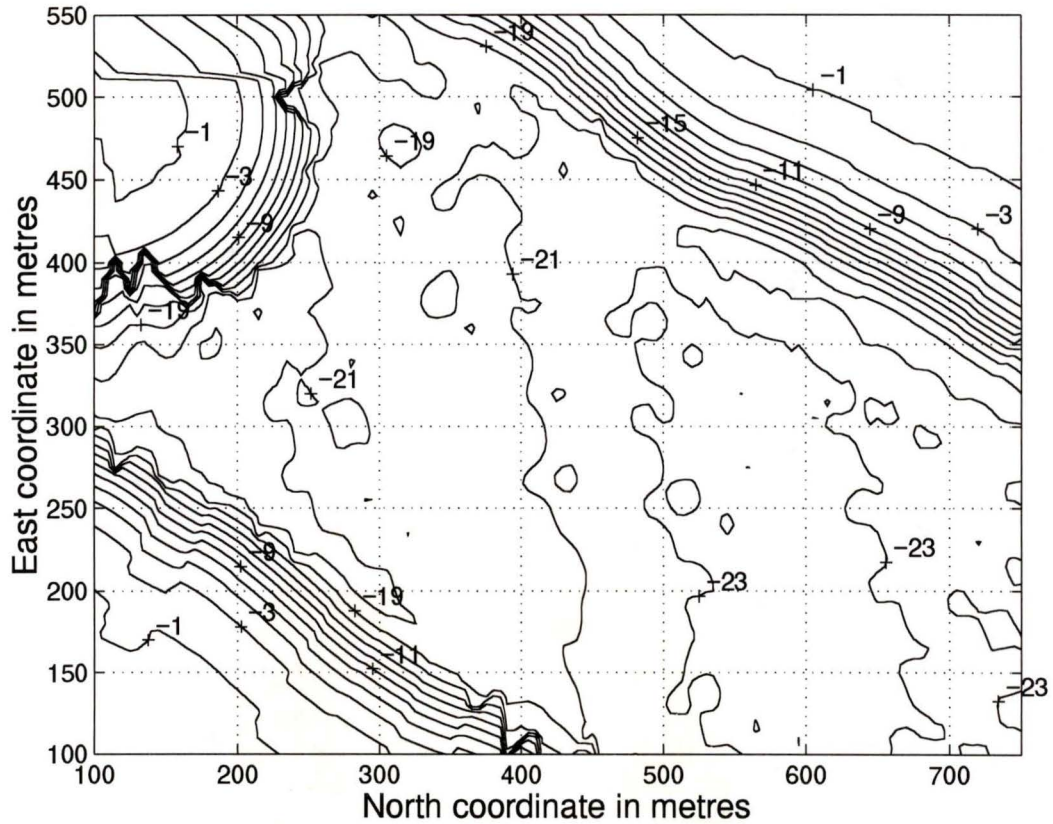


Figure 4.3: Contour map of reconstructed seabed topography by interpolation.

where

$$\mathcal{D}^+ = (\mathcal{D}^T \mathcal{D})^{-1} \mathcal{D}^T$$

From (4.2), it can be observed the depth at the grid point of interest can be obtained directly from the first element of vector \mathbf{A} , i.e., a_0 . In other words,

$$F(X(b^*), Y(b^*)) = a_0$$

The interpolated depth profile can be illustrated by the contour map shown in Figure 4.3.

4.3 Additive Noise Filtering

In this section, attention will be given to the filtering of a given 2-D profile of sea depth that has been degraded by a certain amount of noise. In [20], an algorithm for the removal of additive noise from a degraded image based on the local statistics of the image at hand was proposed. What we report here can be viewed as an application of the method proposed in [20] to 2-D profiles of sea depth. If $z_{i,j}$ is the degraded pixel $x_{i,j}$ in a given 2-D sea depth profile, then

$$z_{i,j} = x_{i,j} + w_{i,j} \quad (4.6)$$

where $w_{i,j}$ denotes the noise which is assumed to satisfy

$$E[w_{i,j}] = 0, \quad E[w_{i,j}w_{k,l}] = \sigma^2\delta_{i,k}\delta_{j,l} \quad (4.7)$$

where $\delta_{i,k}$ is the Kronecker delta function and E is the expectation operator. It is also assumed that the signal $x_{i,j}$ is independent of $w_{i,j}$. The problem is to estimate $x_{i,j}$, given $z_{i,j}$ and the noise statistics. Under these circumstances, we can compute

$$\bar{x}_{i,j} \triangleq E[x_{i,j}] = E[z_{i,j}] = \bar{z}_{i,j} \quad (4.8)$$

and

$$Q_{i,j} \triangleq E[(x_{i,j} - \bar{x}_{i,j})^2] = E[(z_{i,j} - \bar{z}_{i,j})^2] - \sigma^2 \quad (4.9)$$

Like many filtering techniques, the mean and variance of $x_{i,j}$, which are denoted by $\bar{x}_{i,j}$ and $Q_{i,j}$ in (4.8) and (4.9), are computed using the data in a 7×7 window centered at position (i, j) . The noise variance σ^2 can be estimated using data $x_{i,j}$ in a flat region. Using a least-squares approach, we seek to find an optimal unbiased linear estimate of $x_{i,j}$, i.e.,

$$\hat{x}_{i,j} = k_{i,j}z_{i,j} + c_{i,j} \quad (4.10)$$

such that

$$E[\hat{x}_{i,j}] = \bar{x}_{i,j} \quad (4.11)$$

and

$$J = E[\hat{x}_{i,j} - x_{i,j}]^2 \quad (4.12)$$

is minimized. To meet condition (4.11), $c_{i,j}$ must satisfy

$$c_{i,j} = \bar{x}_{i,j}(1 - k_{i,j})$$

and hence (4.10) becomes

$$\hat{x}_{i,j} = (1 - k_{i,j})\bar{x}_{i,j} + k_{i,j}z_{i,j} \quad (4.13)$$

By using (4.12) and (4.13) to solve $\partial J/\partial k_{i,j} = 0$, we obtain

$$k_{i,j} = \frac{Q_{i,j}}{Q_{i,j} + \sigma^2} \quad (4.14)$$

Since $Q_{i,j}$ and σ^2 are both positive, $k_{i,j}$ will lie between 0 and 1. It follows from (4.14) that for a low signal-to-noise ratio region $Q_{i,j}$ is small compared with σ^2 , $k_{i,j} \approx 0$, and the estimated $\hat{x}_{i,j}$ is $\bar{x}_{i,j}$. On the other hand, for a high signal-to-noise ratio region, $Q_{i,j}$ is much larger than σ^2 , $k_{i,j} \approx 1$, and $\hat{x}_{i,j} \approx z_{i,j}$. The use of different window sizes greatly affects the quality of processed images. If the window is too small, the noise filtering algorithm is not effective. If the window is too large, subtle details of the image are lost in the filtering process. As reported in [20], a window size of 7×7 usually leads to satisfactory processing results. The filtered version of the profile of Figure 4.3 is shown in Figure 4.4.

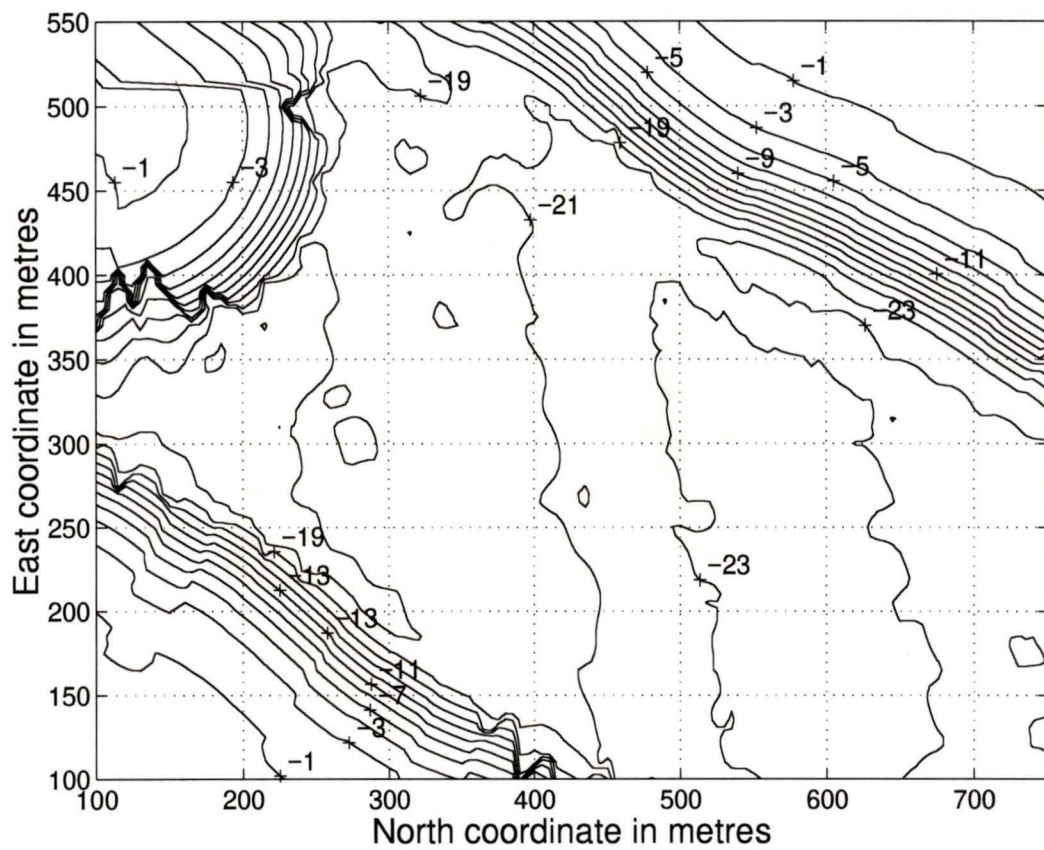


Figure 4.4: Contour map of filtered topography.

4.4 Conclusions

A method for the regularization of 2-D bathymetric data has been implemented using data segmentation and interpolation. The method is straightforward and enables the processing of the data by linear or nonlinear filters. A noise filtering technique by the use of local statistics has then been applied to the regularly spaced data. The outcome is a smoother profile in which wideband noise is removed.

Chapter 5

Conclusions

We have presented several depth estimation and seabed visualization techniques which can lead to significant improvements in the efficiency and reliability of airborne laser ranging systems, in particular, the LARSEN 500 airborne laser bathymeter.

The work begins by considering the raw field waveforms received at the sounding locations in spectral as well as parametric approaches and ends with presenting an accurate representation of the seabed topography. The processing can be broadly divided into two parts. In part I, 1-D processing techniques are used to process laser waveforms individually to obtain improved estimates of sea depth. These depth estimates are then improved further in part II by employing 2-D signal processing techniques. After the application of 1-D and 2-D processing, the resulting depth profiles are considered to be accurate representations of the true seabed topography.

The results achieved are summarized in Section 5.1 and research that can be carried out in the future is described in Section 5.2.

5.1 Results of the Thesis

In Chapter 2, the STDFT has been used in conjunction with a numerical differentiation technique for the estimation of sea depth. This method features the characteristics of bathymetric waveforms in time-frequency domain and makes use of the spectrum to determine sea depth.

In Chapter 3, the introduction of volume backscatter in the existing two-function model (surface and bottom reflections) has made it possible to characterize the surface reflection and volume backscatter separately to reflect the fact that the factors affecting the surface reflection are different from those effecting the volume backscatter. The exponentially modified Gaussian (EMG) function has been found suitable for modeling the volume backscatter. Recursive computation of the EMG as well as the Gaussian functions for modeling the three components has led to a 30 percent reduction in computation. This scheme features modeling the waveforms by parametric functions that have physical meaning.

In Chapter 4, some 2-D digital signal processing techniques have been used to remove noise from the 2-D sea-depth profile. We proposed a method to regularize irregularly spaced data for subsequent 2-D processing. Then the 2-D noise filtering algorithm has been applied to the noisy 2-D data to remove wideband noise.

5.2 Future Studies

Some possible extensions of the results presented in this thesis are now examined. Most of the signal processing techniques developed in the past are based on time-domain analysis. The application of the STDFT to bathymetric waveforms combines

a frequency-domain analysis with a time-domain analysis. This method provides a simple, yet efficient, approach of sea-depth estimation. However, it is also worthwhile to develop an adaptive version of the STDFT as applied to bathymetric data where the size of the window can be varied according to the shape of the waveform at hand.

Another strong interest of Terra Surveys is to explore the potential of the new algorithms developed for the detection of fish schools by using the LIDAR system. The apparent characteristics for the presence of fish schools can be observed from the bulges in the backscatter envelope and the reduced magnitude of return signal from below the level of fish schools. The principle of operation of the LIDAR system for depth estimation is based on the reflection from the water surface and bottom, which are the *targets* of laser pulses. Analogously, the *target* will be the schools of fish if fish detection is of interest. In this regard, some of the feature extraction techniques developed for depth estimation have great potential in terms of transferability to fish detection. Among the techniques, the peak detection methods by using the STDFT and waveform decomposition schemes proposed in the Chapters 2 and 3 could potentially be used to detect the level of fish school in the waters. From some preliminary studies of the problem, it is found that the signal amplitude of the surface peak reflects the density of fish milt while the width of the surface peak relates to water clarity, which has strong correlation to fish schools, spawn or milt. Both indications combined with field videotaping records support the argument of fish presence by observing the bulges appearing on the waveform and form a satisfactory explanation.

Bibliography

- [1] H. Wong, “*Signal processing techniques for airborne laser bathymetry*,” Ph.D. dissertation, University of Victoria, Dec. 1993.
- [2] D. Wells, L. Mayer, and J. E. H. Clarke, “Ocean mapping: From where? To what?,” *CISM Journal ACSGC*, vol. 45, no. 4, pp. 505-518, 1991.
- [3] D. G. Tucker and B. K. Gazey, *Applied Underwater Acoustics*, Pergamon Press, Oxford, 1966.
- [4] G. D. Hickman and J. E. Hogg, “Application of an airborne pulsed laser for near shore bathymetric measurements,” *Remote Sensing Environ.* vol. 1, pp. 47-58, 1969.
- [5] G. C. Guenther and R. W. L. Thomas, “Effects of propagation-induced pulse stretching in airborne laser bathymetry,” *Proceedings of Seventh SPIE Conference on Ocean Optics*, Monterey, CA, pp. 287-296, June 1984.
- [6] K. Muirhead and A. P. Cracknell, “Airborne lidar bathymetry: review articles,” *Int. J. Remote Sensing*, vol. 7, no. 5, pp. 597-614, 1986.

- [7] S. Svanberg, "Lasers as probes for air and sea," *Contemp. Phys.*, vol. 21, No. 6, pp. 541-576, 1980.
- [8] G. C. Guenther, "Airborne Laser Hydrography - System Design and Performance Factors," Tech. Rep., National Ocean and Atmospheric Administration (NOAA), March 1985.
- [9] A. Antoniou, *Digital Filters: Analysis, Design, and Applications.*, Second Edition, McGraw-Hill Co., 1993.
- [10] L. R. Rabiner and R. W. Schafer, *Digital Processing of Speech Signals.*, Englewood Cliff, N.J., Prentice-Hall, 1978.
- [11] L. Cohen, "Introduction: A Primer on Time-Frequency Analysis," in *Time-Frequency Signal Analysis - Methods and Applications*, Boualem Boashash, Ed. John Wiley & Sons, Inc., 1992, Part I, pp. 3-42.
- [12] H. Wong and A. Antoniou, "Characterization and decomposition of waveforms for LARSEN 500 airborne system," *IEEE Trans. Geoscience and Remote Sensing*, vol. 29, pp. 912-921, Nov. 1991.
- [13] H. Wong and A. Antoniou, "One-dimensional signal processing techniques for airborne laser bathymetry," *IEEE Trans. Geoscience and Remote Sensing*, Jan. 1994.
- [14] M. Abramowitz and I. A. Stegun, eds., *Handbook of Mathematical Functions.* Applied Mathematics Series, No. 55, National Bureau of Standards, Washington, D.C., pp. 1779-1784, 1989.

- [15] R. Fletcher, *Practical Methods of Optimization*, Vol. 1, John Wiley, New York, 1980.
- [16] A. Antoniou, *Introduction to Optimization Theory and Practice*, University of Victoria, Dept. of Elec. and Comp. Engr., Apr. 1994.
- [17] W. Cheng, W.-S. Lu, and A. Antoniou, "Efficient waveform decomposition for airborne laser bathymetry," *IEEE Pacific Rim Conference on Communications, Computers, and Signal Processing*, Victoria, B.C., May 17-19, 1995.
- [18] W.-S. Lu and A. Antoniou, *Two-Dimensional Digital Filters*, New York, Marcel Dekker, 1992.
- [19] D. S. Watkins, *Fundamentals of Matrix Computations*, Wiley, pp. 420-421, 1991.
- [20] J.-S. Lee, "Digital image enhancement and noise filtering by use of local statistics," *IEEE Trans. Pattern Anal. and Machine Intelligence*, vol. PAMI-2, no. 2, pp. 165-168, March 1980.

Appendix A

MATLAB Programs for Chapter 2

```

%
% =====
%
%           STDFT.m
%
% =====
%
% This program is implementing the depth estimation algorithm
% on the use of short-time discrete Fourier transform (STDFT)
% method. The detailed algorithm is discussed in chapter 2.
%
% This function loads the waveform data and processes the data
% finally returns the depth corresponding the waveform data.
%
clear;
CPU=cputime;
flops(0);
file_name=input('ENTER THE FILENAME OF THE DATA FILE:   ','s');

while file_name==[],
    file_name=input('ENTER THE FILENAME OF THE DATA FILE:   ','s');
end;

while fopen(file_name,'r')<0,
    disp('
')
    L=['ERROR:  Cannot locate the file,'];
    L=[L,' please specify the full-path'];
    disp(L);
    L=['ELSE: type ''exit'' to quit the program,'];
    L=[L,' return to continue'];
    exit_p=input([L,'  '],'s');
    X=[strcmp(exit_p,'''exit''') | strcmp(exit_p,'EXIT') ];

```

```

XX=[X | strcmp(exit_p, 'EXIT') | strcmp(exit_p, 'quit')];
XXX=[XX | strcmp(exit_p, 'quit') | strcmp(exit_p, 'exit')];
if XXX==1,
    disp('EXIT')
    return;
else
    disp('
    ')
    disp('SAMPLE: /home/wcheng/LIDAR/du1030.mat')
    L=['ENTER THE FULL PATH WITH THE FILENAME: '];
    file_name=input(L, 's');
    while file_name==[],
        file_name=input(L, 's');
    end;
end;
end;
end;
end;
end;
end;
end;
end;

eval(['load ', file_name])
fclose('all');
[row column]=size(sample);

if column==1,
    sc=1;
else
    L=['ENTER THE SERIAL NUMBER OF THE WAVEFORM: '];
    L=[L, '1 to ', num2str(column)];
    sc=input([L, ' '], 's');
end;
sample=sample(:, sc);

% The data format is 256 samples, the window size begins with L and
% Increments by k; ends with M;
L=input('Specify the first window size, default is 3 ');
if L==[], L=3; end;
k=input('Specify the increment step of window size, default is 4 ');
if k==[], k=4; end;
M=input('Specify the last window size, default is 23 ');
if M==[], M=23; end;

% Calculate the first STDFT sample
STFT(1,1)=sum(sample(1:L));

```

```

% Calculate STDFT strings of the first window size
for i=2:row-L+1,
    j=i-1;
    STFT(1,i)=STFT(1,j)-sample(j)+sample(L+j);
end;

% Calculate a set of STDFT strings with various window sizes,
% Number of strings in a set is kk
kk=length(L:k:M);
for p=1:kk,
    q=p+1;
    STFT(q,1)=STFT(p,1)+sum(sample(L+1+k*(p-1):L+k+k*(p-1)));
    for i=2:row-L-k*p+1,
        j=i-1;
        STFT(q,i)=STFT(q,j)-sample(j)+sample(L+k*p+j);
    end;
end;

% normalization and return the result of STDFT sets
S=length(STFT);
STFT1=STFT./([L:k:(p*k)+L]'*ones(1,S));

% Calculate the CPU time and flops required for the calculation
'required for STDFT calculation'
CPU=cputime-CPU, FLOP=flops,

% checking if the STDFT strings obtain two peak positions or
% reach the end of the STDFT strings set
% don't do number of peaks checking
CPU1=cputime; flops(0); e=[1 2 3]; i=1;
while (i<=q) & length(e)~=5,
    dobj=diff(STFT1(i,:));
    I1=find(dobj~=0);
    LI1=length(I1);
    A1=dobj(I1);
    index=I1(find(A1(2:LI1-1)./A1(1:LI1-2)<0)+1);
    e=index(find(dobj(index)<0)),
    g=index(find(dobj(index)>0));
    i=i+1;
end;

```

```
% spurious peak pick-out
if length(e)==2,
[MM index]=max(sample(1:e(2)));
x=e(2)-e(1)+index;
if sample(x)<=4,
x=-100,
end;
% ii,
[x e(1) e(2) index]
pause(5)
else x=-100,
end;

% Calculate the CPU time and flops required for the
% calculation
'required for differentiation'
CPU1=cputime-CPU1, FLOP1=flops,
'required for the total programming'
CPU=CPU+CPU1, FLOP=FLOP+FLOP1,
```

```

% =====
%     Figure 2.1
% =====

load ../../tmp/prep/demo_wei/sample1
[row column]=size(sample);
% x=[0:row-1;0:255]';
% t=[zeros(row,1) sample];
subplot(211);
line(0:row-1,sample);
axis([0 255 0 150])
M=['|<----- 512 nsec'];
L=[M,' ----->|'];
xlabel(L);
subplot(212);
inter=1;
hold on
axis([0 255 0 150])
for i=1:inter:row,
line([i,i],[0 sample(i)]);
% line(x(i,:),t(i,:));
end;
M=['|<----- 256 samples'];
L=[M,' ----->|'];
xlabel(L);
hold off
print -deps AtoD.eps

% =====
%     Figure 2.2
% =====
%
load ../../tmp/prep/demo_wei/sample1.mat
clear set
subplot(211)
plot(sample)
axis([0 255 0 200])
grid
xlabel('sample index','fontsize',12);

```

```

ylabel('signal magnitude','fontsize',12);
text(128,-50,'(a)','fontsize',12);
DFT=abs(fft(sample));
subplot(212)
plot(0:2*pi/length(sample):2*pi,[DFT;DFT(1)]);
axis([0 2*pi 0 max(DFT)])
grid
text(2.6,-550,'frequency','fontsize',12)
ylabel('spectrum magnitude','fontsize',12)
set(gca,'xtick',[ ]);
text(6.14,-300,'2p','fontname','symbol','fontsize',12)
text(0,-300,'0','fontname','symbol','fontsize',12)
text(3.1,-300,'p','fontname','symbol','fontsize',12)
text(3.1,-1100,'(b)','fontsize',12);
hold on
plot([3.14*ones(51,1)],[0:max(DFT)/50:max(DFT)],'.','markersize',2)
hold off
print -deps figch22.eps

% =====
%      Figure 2.3
% =====

load ../tmp/prep/demo_wei/sample1.mat
clear set
L=16;
row=length(sample);
for i=1:row-L+1,
STFT(:,i)=sample(i:i+L-1);
end;
STDFT=abs(fft(STFT));
mesh(1:row-L+1,0:2*pi/L:2*pi,[STDFT; STDFT(1,:)])/L);
shading interp
AA=max(max(STDFT/L));
axis([0 row-L+1 0 2*pi 0 AA]);
grid
xlabel('sample index','fontsize',12)
text(-100,3.1,0,'frequency','fontsize',12)
zlabel('normalized spectrogram magnitude','fontsize',12)
set(gca,'ytick',[])
text(-30,2.6,0,'p','fontname','symbol','fontsize',12)

```

```

text(-30,5.6,0,'2p','fontname','symbol','fontsize',12)
text(-30,-0.5,0,'0','fontname','symbol','fontsize',12)
set(gca,'fontsize',12);
hold on
plot3(241*ones(51,1),[pi*ones(51,1)],[0:AA/50:AA],'.','markersize',2)
plot3(241*ones(51,1),[2*pi*ones(51,1)],...
      [0:AA/50:AA],'.','markersize',2)
plot3(241*ones(51,1),[zeros(51,1)],[0:AA/50:AA],'.','markersize',2)
hold off
print -deps spectro.eps

% =====
%   Figure 2.4
% =====

load ../../tmp/prep/demo_wei/sample1.mat
clear set
ss=0.5; L=16;
row=length(sample);
for i=1:row-L+1,
STFT(:,i)=sample(i:i+L-1);
end;
STDFT=abs(fft(STFT));
subplot(221)
aa=0:1:row-1;
plot(aa,[STDFT(1,:)/L zeros(1,L-1)],'-',...
      aa,sample,':','markersize',ss);
grid
axis([0 255 0 140]);
xlabel('sample index','fontsize',12)
ylabel('magnitude','fontsize',12)
text(128,-40,'(a)','fontsize',12)

subplot(222)
aa=0:1:row-1;
plot(aa,[STDFT(9,:)/L zeros(1,L-1)],'-',...
      aa,sample,':','markersize',ss);
grid
axis([0 255 0 140]);
xlabel('sample index','fontsize',12)
ylabel('magnitude','fontsize',12)

```

```

text(128,-40,'(b)', 'fontsize',12)

subplot(223)
aa=0:1:row-1;
plot(aa,[STDFT(2,:)/L zeros(1,L-1)], '--', ...
      aa,sample, ':', 'markersize',ss);
grid
axis([0 255 0 140]);
xlabel('sample index', 'fontsize',12)
ylabel('magnitude', 'fontsize',12)
text(128,-40,'(c)', 'fontsize',12)

subplot(224)
aa=0:1:row-1;
plot(aa,[STDFT(16,:)/L zeros(1,L-1)], '--', ...
      aa,sample, ':', 'markersize',ss);
grid
axis([0 255 0 140]);
xlabel('sample index', 'fontsize',12)
ylabel('magnitude', 'fontsize',12)
text(128,-40,'(d)', 'fontsize',12)
print -deps pissection.eps

% =====
%   Figure 2.5
% =====

load ../../tmp/prep/demo_wei/sample1.mat
clear set
ss=0.2; row=length(sample);
L=3;
clear STFT
for i=1:row-L+1,
STFT(:,i)=sample(i:i+L-1);
end;
STDFT=sum(STFT)/L;
subplot(221)
aa=0:1:row-1;
plot(aa,[STDFT zeros(1,L-1)], '--', ...
      aa,sample, ':', 'markersize',ss);
grid

```

```
axis([0 255 0 140]);
xlabel('sample index','fontsize',12)
ylabel('magnitude','fontsize',12)
text(128,-40,'(a)','fontsize',12)
```

```
L=7;
clear STFT
for i=1:row-L+1,
STFT(:,i)=sample(i:i+L-1);
end;
STDFT=sum(STFT)/L;
subplot(222)
aa=0:1:row-1;
plot(aa,[STDFT zeros(1,L-1)],'-',...
      aa,sample,':','markersize',ss);
grid
axis([0 255 0 140]);
xlabel('sample index','fontsize',12)
ylabel('magnitude','fontsize',12)
text(128,-40,'(b)','fontsize',12)
```

```
L=11;
clear STFT
for i=1:row-L+1,
STFT(:,i)=sample(i:i+L-1);
end;
STDFT=sum(STFT)/L;
subplot(223)
aa=0:1:row-1;
plot(aa,[STDFT zeros(1,L-1)],'-',...
      aa,sample,':','markersize',ss);
grid
axis([0 255 0 140]);
xlabel('sample index','fontsize',12)
ylabel('magnitude','fontsize',12)
text(128,-40,'(c)','fontsize',12)
```

```
L=15;
clear STFT
for i=1:row-L+1,
STFT(:,i)=sample(i:i+L-1);
```

```
end;
STDFT=sum(STFT)/L;
subplot(224)
aa=0:1:row-1;
plot(aa,[STDFT zeros(1,L-1)],'-',...
      aa,sample,':','markersize',ss);
grid
axis([0 255 0 140]);
xlabel('sample index','fontsize',12)
ylabel('magnitude','fontsize',12)
text(128,-40,'(d)','fontsize',12)
print -deps windowsize.eps
```

Appendix B

MATLAB Programs for Chapter 3

```

%
% =====
%           wd1.m
% =====
%
% This main program implements the waveform decomposition algorithm
% discussed in the Chapter 3 of the thesis. The algorithm decompose
% a bathymetric waveform into three components characterizing the
% surface reflection, volume backscatter, and bottom reflection
% which are sequentially implemented in this software program.
%
% GLOBAL VARIABLES:
%
% OBJ    /* the sample values used in each optimization */
% nni    /* the beginning sample point */
% nne    /* the ending sample point */
% row    /* the number of sample points in a single waveform */
% data   /* the sample values smoothed by 12-th order FIR filter */
%
clear
flops(0)
global OBJ nni nne row data

% *****
% load data file and check keyboard input
% *****

file_name=input('ENTER THE FILENAME OF THE DATA FILE:   ','s');

while file_name==[],
    file_name=input('ENTER THE FILENAME OF THE DATA FILE:   ','s');
end;

while fopen(file_name,'r')<0,

```

```

disp('
')
L=['ERROR: Cannot locate the file,'];
L=[L,' please specify the full-path'];
disp(L);
L=['ELSE: type ''exit'' to quit the program,'];
L=[L,' return to continue'];
exit_p=input([L,' '], 's');
X=[strcmp(exit_p,'''exit''') | strcmp(exit_p,'EXIT') ];
XX=[X | strcmp(exit_p,'''EXIT''') | strcmp(exit_p,'quit')];
XXX=[XX | strcmp(exit_p,'''quit''') | strcmp(exit_p,'exit')];
if XXX==1,
    disp('EXIT')
    return;
else
    disp('
')
    disp('SAMPLE: /home/wcheng/LIDAR/du1030.mat')
    L=['ENTER THE FULL PATH WITH THE FILENAME: '];
    file_name=input(L,'s');
    while file_name==[],
        file_name=input(L,'s');
    end;
    % end while file_name==[]
end;
    % end if XXX==0
end;
    % end while fopen('file_name','r')<0

eval(['load ', file_name])
fclose('all');
[row column]=size(sample);
CPU=cputime;
% *****
if column==1,
    sc=1;
else
    L=['ENTER THE SERIAL NUMBER OF THE WAVEFORM: '];
    L=[L,'1 to ',num2str(column)];
    sc=input([L,' '], 's');
end;
data1=sample(:,sc);
[Sur Bot Bot1 BoT1]=gobs1f(sc,data1);
data=smooth1(data1,12,0.001);

```

```

% =====
% Description:
%
% This part is modeling the surface reflection by EMG (exponentially
% modified Gaussian) function
% Functions required:
%
% bfgs1.m      /* the BFGS optimization driver */
% YEMG.m       /* calculate the EMG function values on returning
%               the column vector of four elements
%               hG, sigmaG, tau, tG */
%
if exist('x_star1')~=1,
    x01=[7 3.5 30]'
else
    x01=x_star1(2:4)
end;
epsilon1=1e-4;
nni=1;
nne=Sur+7
OBJ=data(nni:nne);
[x_star1 k1]=bfgs1(x01,epsilon1);
save x_star1 x_star1;
yemg1=YEMG(x_star1);
bs=data'-yemg1;
a=0:1:255;
plot(a,bs', '-.',a,yemg1', '. ',a,data, '-');
axis([0 255 min(bs) 150]);
p1=[ ];
for i=1:length(x_star1),
    p1=[p1 ' ' num2str(x_star1(i))];
end;
xlabel(['Waveform serial # ',num2str(sc)]);
ylabel('Magitude')
title(['x_star1 = ',p1,']);
grid
pause(3)

```

```

% =====
% Description:
%
% This part is modeling the volume backscatter by EMG
% (exponentially modified Gaussian) function
% Functions required:
%
% bfgs1.m          /* the BFGS optimization driver */
% YEMG.m           /* calculate the EMG function values on returning
%                  the column vector of four elements
%                  hG, sigmaG, tau, tG */
%
% *****
% search for the skeleton of the profile of volume backscatter
% by polynomial interpolation of order 4, order 4 is enough,
% although increasing order can obtain better results, but the
% FLOPS required is not worth for the order increasing
p=find(bs1(31:nni)>0); p=p+30;
[p1 S]=polyfit(p,bs1(p),4);
[y1 delta]=polyval(p1,p,S);
y2=[zeros(30,1); y1; zeros(256-length(y1)-30,1)];
y3=smooth(y2,12,0.01);
plot([data yemg1' YG' y3])
plot(a,data,'-.',a,yemg1','.',a,YG','-',a,y3,'--')
axis([0 255 0 200])
grid
% *****

[m33 p33]=max(y3);
if exist('x_star3')~=1,
%   x03=[4 2.5 3]'
   x03=[.5 20 1]'
else
   x03=x_star3(2:4)
end;
epsilon3=1e-4;
nni=1;
nne=256;

```

```

OBJ=y3(nni:nne);
[x_star3 k3]=bfgs1(x03,epsilon3)
save x_star3 x_star3;
x03=x_star3(2:4)
[x_star3 k3]=bfgs1(x03,epsilon3)
yemg2=YEMG(x_star3);
plot(a,data,'-.',a,yemg1','.',a,YG','-',a,yemg2,'--')
axis([0 255 0 200])
grid
CPU=cputime-CPU;
FLOPS=flops;

% =====
% Description:
%
% This part is modeling the bootom reflection by Gaussian function
% Functions required:
%
% bfgs2.m      /* the BFGS optimization driver */
% obj2.m       /* calculate the Gassian function values by the
%               the column vector of three elements
%               Amax, tmax, sigma */
%
nni=BoT1-5;
nne=BoT1+10;
OBJ=bs(nni:nne)';
x02=[max(OBJ) BoT1 3]';
epsilon2=1e-4;
[x_star2 k2]=bfgs2(x02,epsilon2);
save x_star2 x_star2
[z YG]=obj2(x_star2);
bs1=(bs-YG)';
plot([YG' yemg1' data]);
AXIS=[0 255 min(min([YG' yemg1' data])) max(max([YG' yemg1' data]))];
axis(AXIS);
grid;
p2=[ ];
for i=1:1:length(x_star2),
p2=[p2 ' ' num2str(x_star2(i))];
end;

```

```
title(['x_star2 = ',p2,']');
xlabel(['Waveform serial # ',num2str(sc)] )
pause(3)

% =====
%
%      smooth1.m
%
% =====
%
% This function returns a sequence of data after the lowpass
% filtering by FIR filter of impulse response specified in "b"
% vector.  And the lowpass filtered data are returned in "f".
%
function f=smooth1(data1)
b=1/143*[-11 0 9 16 21 24 25 24 21 16 9 0 -11];
ode=(length(b)-1);
f=filter(b,1,data1);
f=[f(ode/2+1:length(data1)) ; zeros(ode/2,1)];
```

```

%
% =====
%                bfgs1.m
% =====
%
% This function is implementing the quasi-Newton optimization
% with the BFGS updating formula to obtain an optimal set of
% parameters for the surface reflection which is characterized
% by the EMG function discussed in the Chapter 3.
%
% This Matlab-function is a second level program directly used
% by the main software program for waveform decomposition named
% as wd1.m.
%
% [x_star,k]=bfgs1(x0,epsilon) returns the optimal set of
% values for the parameters, x_star, the iteration number, k;
% where x0 is the initial value, and epsilon is the termination
% criterion, 1e-4.
%

function [x_star,k]=bfgs1(x0,epsilon)
global OBJ nni nne data row
x=x0;
X=x0;
k=1;
F(1)=func1(x);
current_status=[1 F(1)]
d=1;
H=eye(length(x));
g=gra1(x);
STOP=0;
plus1=0;
while (d > epsilon) & (~STOP),
s=-H*g;
alpha=f1s(x,s,'func1','gra1');
dt=alpha*s;
x=x+dt;
if k>1,
G1=abs((F(k)-F(k-1)))/F(k)
G2=(X(2,k)-X(2,k-1))
end;

```

```

if (k==1) & (find(x<=0)~=[])
    STOP=1;
    k
elseif (find(x<=0)~=[]) | ((x(2)>10) & G2>2) | (G1<=.5*1e-4),
    STOP=1;
    x
else
    X=[X x];
    x1=x
    [ze zJ zyemg]=wdfun1(x1);
    plot([OBJ zyemg'])
    pause(3);
    hG=HG(x1);
    yemg=YEMG([hG; x1]);
    plot([data yemg']);
    pause(3);
end;
g1=gra1(x);
ga=g1-g;
g=g1;
if (~STOP),
    k=k+1,
    F(k)=func1(x);
    current_status=[k F(k)]
end;
d=norm(dt);
if (k/length(x)-ceil(k/length(x)) < 0),
    v1=H*ga;
    v2=ga'*dt;
    v3=v1*dt';
    H=H+((v2+ga'*v1)/(v2^2))*(dt*dt')-(v3+v3')/v2;
else
    H=eye(length(x0));
end;
end;
if (x(2)>10 & G2>2),
    plus1=1;
    hG=HG(x);
    x_star=[hG; x];
else
    [ze zJ zyemg]=wdfun1(X(:,k));

```

```
plot([OBJ zyemg'])
pause(3)
hG=HG(X(:,k));
x_star=[hG X(1,k) X(2,k) X(3,k)]';
end;
```

```

%
% =====
%                bfgs2.m
% =====
%
% This function is implementing the quasi-Newton optimization
% with the BFGS updating formula to obtain an optimal set of
% parameters for the bottom reflection which is characterized
% by the Gaussian function discussed in the Chapter 3.
%
% This Matlab-function is a second level program directly used
% by the main software program for waveform decomposition named
% as wd1.m.
%
% [x_star,k]=bfgs2(x0,epsilon) returns the optimal set of values
% for the parameters, x_star, the iteration number, k; where x0
% is the initial value, and epsilon is the termination criterion,
% 1e-4.
%

function [x_star, k]=bfgs2(x0,epsilon)
global OBJ nni nne
nn=length(OBJ);
x=x0;
X=x0;
k=1;
F(1)=func2(x);
current_status=[1 F(1)]
d=1;
H=eye(length(x));
g=gra2(x);
STOP=0;
while (d > epsilon) & (~STOP),
s=-H*g;
alpha=f1s(x,s,'func2','gra2');
dt=alpha*s;
x=x+dt;
if (find(x<=0)~=[]),
    STOP=1;
else
    X=[X x];

```

```
x1=[x(1) x(2) x(3)]'  
[ze zJ zyG]=wdfun2(x1);  
plot([OBJ zyG'])  
pause(3);  
end;  
g1=gra2(x);  
ga=g1-g;  
g=g1;  
if (~STOP),  
    k=k+1;  
    F(k)=func2(x);  
    current_status=[k F(k)]  
end;  
d=norm(dt);  
if (k/7-ceil(k/7) < 0),  
    v1=H*ga;  
    v2=ga'*dt;  
    v3=v1*dt';  
    H=H+((v2+ga'*v1)/(v2^2))*(dt*dt')-(v3+v3')/v2;  
else  
    H=eye(length(x0));  
end;  
end;  
x_star=[X(1,k) X(2,k) X(3,k)]';  
[ze zJ zyG]=wdfun2(x_star);
```

```

%
% =====
%          func1.m
% =====
%
%
% This function returns the squared value of the weighted objective
% function formed by the difference between the sample values and the
% values calculated from the EMG function model.
%
% The objective function is returned by obj1.m labeled as "ze", and
% apply appropriate weights to get the weighted objective function
% "we". The saured value of the weighted objective function is then
% obtained by column-wise multiplication
%
%          z=we .* we = we * we'
%
% where "we'" is the transpose of row vector "we".
%
%
% This Matlab-function is a third level program used by the bfgs1.m
% for waveform decomposition to evaluate the sqaured value of the
% weighted objective function.
%
% z=func1(x) returns the z value which is the column-wise product
% (squared) value of the weighted objective function. x is a vector
% that contains the second to fourth parameters of the EMG function.
%

function z=func1(x)
global OBJ nni nne
ze=obj1(x);
we=ze.*[ones(1,nne-6-nni+1) 5*ones(1,3) 10*ones(1,3)];
z=we*we';

```

```
%
% =====
%          func2.m
% =====
%
%
% This function returns the squared value of the objective function
% formed by the difference between the sample values and the values
% calculated from the Gaussian function model.
%
% This Matlab-function is a third level program used by the bfgs2.m
% for waveform decomposition.
%
% z=func2(x) returns the z value which is the component-wise product
% (squared) value of the weighted objective function. x is a vector
% of the objective function.
%

function z=func2(x)
global OBJ inn enn
ze=obj2(x);
z=ze*ze';
```

```

%
% =====
%          gra1.m
% =====
%
% This function retruns the gradient vector of the squared value of
% the weighted objective function formed by the difference between
% the sample values and the values calculated from the EMG function.
%
%
% The objective function and the Jacobian matrix are returned by
% wdfun1.m labeled as "ze" and "zJ". And then apply appropriate
% weights to get the weighted objective function and the weighted
% Jacobian matrix labeled as "we" and "wJ". The gradient vector of
% the squared value of the weighted objective function is then
% obtained by the following operation
%
%          z=2 * wJ * we'
%
% where "we'" is the transpose of row vector "we".
%
%
% This Matlab-function is a third level program used by the bfgs1.m
% for waveform decomposition to evaluate the gradient of the squared
% value of the weighted objective function.
%
% z=gral(zx) returns the z vector which is the gradient vector of the
% squared value of weighted objective function. y is sample values
% and the values calculated from the EMG waveform model.
% zx is a vector that contains the second to fourth parameters of the
% EMG function.
%
function z=gral(zx)
global OBJ nni nne
[ze zJ zF]=wdfun1(zx);
we=ze.*[ones(1,nne-6-nni+1) 5*ones(1,3) 10*ones(1,3)];
wJ=zJ.*[ones(3,nne-6-nni+1) 5*ones(3,3) 10*ones(3,3)];
z=2*wJ*we';

```

```

%
% =====
%           gra2.m
% =====
%
% This function retruns the gradient vector of the squared value of
% the weighted objective function formed by the difference between
% the sample values and the values calculated from the Gaussian
% function.
%
% The objective function and the Jacobian matrix are returned by
% wdfun2.m labeled as "ze" and "zJ". The gradient vector of
% the squared value of the weighted objective function is then
% obtained by the following operation
%
%           z=2 * zJ * ze'
%
% where "ze'" is the transpose of row vector "ze".
%
%
% This Matlab-function is a third level program used by the bfgs2.m
% for waveform decomposition to evaluate the gradient of the squared
% value of the weighted objective function.
%
% z=gra2(zx) returns the z vector which is the gradient vector of the
% squared value of weighted objective function. y is sample values
% and the values calculated from the Gaussian function. zx is a
% vector that contains the parameters of the Gaussian function.
%
function z=gra2(zx)
global OBJ inn enn
[ze zJ zyG]=wdfun2(zx);
z=2*zJ*ze';

```

```

%
% =====
%           HG.m
% =====
%
% This function is implementing the recursive formula derived in the
% Chapter 3 for the Exponentially modified Gaussian (EMG) function
% and obtain the first parameter hG based on sigmaG, tau, tG , and
% the peak value and peak position of the EMG function that model
% the waveform of interest.
%
% This Matlab-function is a third level program used by the bfgs1.m
% for waveform decomposition.
%
% hG=HG(GG) returns the first parameter hG based on the other three
% parameters formed in vector "GG" and the waveform samples "OBJ".
%

function hG=HG(GG)
global OBJ
sigmaG=GG(1);
tau=GG(2);
tG=GG(3);
[P tp]=max(OBJ);
ther=5;
CT=sqrt(2*pi);
zp=(tp-tG)/sigmaG-sigmaG/tau;
if (zp > ther),
    Izp=CT;
else
    Izp=quad8('func',0,zp)+CT/2;
end;
C00=sigmaG/tau;
C0=P*exp(tp/tau)/Izp;
hG=C0/C00/exp(C00^2/2+tG/tau);

```

```

%
% =====
%           YEMG.m
% =====
%
% This function is implementing the recursive formula derived in the
% Chapter 3 for the Exponentially modified Gaussian (EMG) function
% based on the available four parameters hG, sigmaG, tau, and tG.
%
% This Matlab-function is a third level program used by the bfgs1.m
% for waveform decomposition to evaluate the EMG function values.
%
% yemg2=YEMG(x) returns the EMG function values yemg2 based on the
% available four parameters formed in x.
%

function yemg2=YEMG(x)
global nni nne row
hG=x(1);
sigmaG=x(2);
tau=x(3);
tG=x(4);
p=.231642;
b=[.319382 -.356564 1.78148 -1.82126 1.33027];
C00=sigmaG/tau;
C0=sqrt(2*pi)*hG*exp(C00^2/2+tG/tau)*C00;
C4=exp(-1/tau);
C8=1/sigmaG;
C5=exp(-C8);
C6=C5^C8;
C7=exp(-C8^2/2);
C9=tG/sigmaG+C00;
a=exp(-C9^2/2)/sqrt(2*pi);
q=1/(1+p*C9);
q2=q^2;
q4=q2^2;
AB=a*(b*[q q2 q2*q q4 q4*q]');
zz=-C9;
yemg1=C0;
if zz <= 0,

```

```
    yemg(1)=yemg1*AB;
else
    yemg(1)=yemg1*(1-AB);
end
C5k=C5^(-(C8+C9));
for i=1:row-nni,
    j=i+1;
    yemg1=C4*yemg1;
    zz=zz+C8;
    C5k=C5k*C6;
    a=a*C5k*C7;
    q=1/(1+p*abs(zz));
    q2=q^2;
    q4=q2^2;
    AB=a*(b*[q q2 q2*q q4 q4*q]');
    if zz <= 0,
        yemg(j)=yemg1*AB;
    else
        yemg(j)=yemg1*(1-AB);
    end
end
yemg2=[zeros(1,nni-1) yemg];
```

```

%
% =====
%           obj1.m
% =====
%
% This function is implementing the recursive formula derived in the
% Chapter 3 for the Exponentially modified Gaussian (EMG) function.
%
% This Matlab-function is a fourth level program used by the func1.m
% for waveform decomposition.
%
% z=obj1(y) returns the z vector which is the objective function
% that is the difference between the sample values and the values
% calculated from the EMG waveform model. y is a vector that
% contains the second to fourth parameters of the EMG function.
%

function z=obj1(y)
global OBJ hG nni nne
sigmaG=y(1);
tau=y(2);
tG=y(3);
p=.231642;
b=[.319382 -.356564 1.78148 -1.82126 1.33027];
[P tp]=max(OBJ);
ther=5;
CT=sqrt(2*pi);
zp=(tp-tG)/sigmaG-sigmaG/tau;
if (zp > ther),
    Izp=CT;
else
    Izp=quad8('func',0,zp)+CT/2;
end;
C00=sigmaG/tau;
C0=P*exp(tp/tau)/Izp;
C4=exp(-1/tau);
C8=1/sigmaG;
C5=exp(-C8);
C6=C5^C8;

```

```

C7=exp(-C8^2/2);
C9=tG/sigmaG+C00;
a=exp(-C9^2/2);
q=1/(1+p*C9);
q2=q^2;
q4=q2^2;
AB=a*(b*[q q2 q2*q q4 q4*q]');
zz=-C9;
yemg1=C0;
if zz > ther,
    yemg(1)=yemg1*CT;
elseif zz > 0,
    yemg(1)=yemg1*(CT-AB);
else
    yemg(1)=yemg1*AB;
end
C5k=C5^(-(C8+C9));
for i=1:nne-nni,
    j=i+1;
    yemg1=C4*yemg1;
    zz=zz+C8;
    C5k=C5k*C6;
    a=a*C5k*C7;
    q=1/(1+p*abs(zz));
    q2=q^2;
    q4=q2^2;
    AB=a*(b*[q q2 q2*q q4 q4*q]');
    if zz > ther,
        yemg(j)=yemg1*CT;
    elseif zz > 0,
        yemg(j)=yemg1*(CT-AB);
    else
        yemg(j)=yemg1*AB;
    end
end
end
z=yemg-OBJ';

```

```
%
% =====
%          obj2.m
% =====
%
% This function is implementing the recursive formula derived in the
% Chapter 3 for the Gaussian function.
%
% This Matlab-function is a fourth level program used by the func2.m
% for waveform decomposition.
%
% z=obj2(y) returns the z vector which is the objective function
% that is the difference between the sample values and the values
% calculated from the Gaussian waveform model. y is a vector that
% contains the three parameters of the Gaussian function.
%

function z=obj2(y)
global OBJ nni nne row
Amax=y(1);
tmax=y(2);
sigma=y(3);
yG=zeros(1,256);
KK=1:1:row;
yG=Amax*exp(-(KK-tmax).^2/(2*sigma^2));
z=yG(nni:nne)-OBJ';
```

```

% =====
%           wdfun1.m
% =====
%
% This function is implementing the recursive formula derived in the
% Chapter 3 for the Exponentially modified Gaussian (EMG) function
% and the gradient with respect to its parameters hG, sigmaG, tau,
% and tG.
%
% This Matlab-function is a fourth level program used by the gra1.m
% for waveform decomposition.
%
% [e, J, yemg]=wdfun1(GG) returns the Jacobian matrix "J" and the
% objective function "e" formed by the difference between the
% sample values and the calculated EMG function value returned by
% "yemg". GG is a vector of second to fourth parameters of the
% EMG function.

function [e, J, yemg]=wdfun1(GG)
global OBJ hG nni nne
nnn=length(OBJ);
sigmaG=GG(1);
tau=GG(2);
tG=GG(3);
p=.231642;
b=[.319382 -.356564 1.78148 -1.82126 1.33027];
[P tp]=max(OBJ);
ther=5;
CT=sqrt(2*pi);
zp=(tp-tG)/sigmaG-sigmaG/tau;
if (zp > ther),
    Izp=CT;
else
    Izp=quad8('func',0,zp)+CT/2;
end;
C00=sigmaG/tau;
C0=P*exp(tp/tau)/Izp;
C4=exp(-1/tau);
C8=1/sigmaG;
C5=exp(-C8);

```

```

C6=C5^C8;
C7=exp(-C8^2/2);
C9=tG/sigmaG+C00;
a=exp(-C9^2/2);
q=1/(1+p*C9);
q2=q^2;
q4=q2^2;
AB=a*(b*[q q2 q2*q q4 q4*q]');
zz=-C9;
yemg1=C0;
yemg1I(1)=yemg1*a;
if zz > ther,
    yemg(1)=yemg1*CT;
elseif zz > 0,
    yemg(1)=yemg1*(CT-AB);
else
    yemg(1)=yemg1*AB;
end
C5k=C5^(-(C8+C9));
for i=1:nne-nni,
    j=i+1;
    yemg1=C4*yemg1;
    zz=zz+C8;
    C5k=C5k*C6;
    a=a*C5k*C7;
    q=1/(1+p*abs(zz));
    q2=q^2;
    q4=q2^2;
    AB=a*(b*[q q2 q2*q q4 q4*q]');
    if zz > ther,
        yemg(j)=yemg1*CT;
    elseif zz > 0,
        yemg(j)=yemg1*(CT-AB);
    else
        yemg(j)=yemg1*AB;
    end
    yemg1I(j)=yemg1*a;
end
e=yemg-0BJ';
KK=1-1:1:nne-nni;
pztG=-1/sigmaG;

```

```

pzsigmaG=(tG-KK)/sigmaG^2-1/tau;
pzsigmaG1=(tp-tG)/sigmaG^2+1/tau;
pztau=sigmaG/tau^2;
pztau1=(KK-tp)/tau^2;
DR=exp(-zp^2/2)/Izp;
g2=yemg*DR*pzsigmaG1+pzsigmaG.*yemg1I;
g3=yemg.*(pztau1-pztau*DR)+pztau*yemg1I;
g4=-yemg*pztG*DR+pztG*yemg1I;
J=[g2; g3; g4];

% =====
%           wdfun2.m
% =====
%
% This function is implementing the recursive formula derived in the
% Chapter 3 for the Gaussian function and the gradient with respect
% to its parameters Amax, tmax and sigma.
%
% This Matlab-function is a fourth level program used by the gra2.m
% for waveform decomposition.
%
% [e, J, yG]=wdfun2(y) returns the Jacobian matrix "J" and the
% objective function "e" formed by the difference between the
% sample values and the calculated Gaussian value returned by
% "yG".
%
function [e, J, yG]=wdfun2(GG)
global OBJ nni nne
Amax=GG(1);
tmax=GG(2);
sigma=GG(3);
yG=zeros(1,256);
KK=nni-1:1:nne-1;
yG=Amax*exp(-(KK-tmax).^2/(2*sigma^2));
e=yG-OBJ';
pz=(KK-tmax)/sigma^2;
g5=yG/Amax;
g6=yG.*pz;
g7=yG.*pz.^2*sigma;
J=[g5; g6; g7];

```

```

% =====
%   func.m
% =====
%
% This function is used by HG.m obj1.m wdfun1.m to do numerical
% integration of the fun.m for the evaluation of I(z) mentioned
% in Chpater 3.
%

function yy=func(xx)
global tp tG sigmaG tau;
yy=exp(-xx.^2/2);

%
% =====
%   fls.m
% =====
%

function result=fls(x,s,F,G,p1,p2,p3,p4,p5,p6,p7)
% Fletcher's line search algorithm: by Doug Peters, 20 June, 1991
%
% usage: fls(x,s,F,G[,p1[,p2...]])
%   x: initial point
%   s: search direction
%   F: function (horizontal string such as 'rosenbrock')
%   G: function (as above. N.B. F.m & G.m better exist!)
%   px: parameter definitions (e.g. 'rho=.1')
%
%   returns acceptable 'alpha' or distance along search direction s
%
% useful p's include:                                default: pg:
% 'rho=' defines right bracket.                       .25 27
% 'sigma=' defines left bracket. (sigma>rho)           .5 27
% 'al=' first guess for alpha.                        1e-4 34
% 'ftau1=' defines max step for bracketing             9 34
% 'ftau2=' defines min step for sectioning (ftau2<=sigma).1 36
% 'ftau3=' defines max step for sectioning             .5 36
% 'fbar=' defines "absolute lower bound"              0 34

```

```

%
% examples: al = fls(x,s,'myfun','mygrad','fbar=-21','al=1e-5');
%           x = x+fls(x,s,'rose-f','rose-g')*s;

% fbar is the expected minimum limit on the function
% for minimum mean-squared error, zero is the natural choice
fbar=0; epsil=1e-10;
rho=.25; sigma=.5;
% in general, sigma should be bigger than rho (pg. 29)
ftau1=9; ftau2=.1; ftau3=.5; % suggested values (pg. 34 & 36)
% evaluate function and directional derivative at x
eval(['f0=' F '(x);']); fl=f0;
eval(['gg=' G '(x);']); g0=gg*s; gl=g0; g=g0;
% evaluate given parameters:
if nargin>4, eval([p1 ';']);
    if nargin>5, eval([p2 ';']);
        if nargin>6, eval([p3 ';']);
            if nargin>7, eval([p4 ';']);
                if nargin>8, eval([p5 ';']);
                    if nargin>9, eval([p6 ';']);
                        if nargin>10, eval([p7 ';']);
end, end, end, end, end, end, end
% find a suitable first guess for alpha (?)
all=0;
if abs(g0)>epsil,
    al=min([1 2*(fbar-f0)/g0]);
    mu=(fbar-f0)/(rho*g0); % (pg. 34)
else
    al=1;
    mu=1/rho;
end
% find right limit on bracket
% bracketing phase
done=0;
while 1,
% evaluate the function value at alpha
    eval(['f=' F '(x+al*s);']);
    if f<fbar, % we are lower than our absolute lower limit!
        a0=al; b0=al; done=1;
        'lower than absolute lower limit'
        break,

```

```

end
if (f>(f0+rho*al*g0)) + f>=fl, % first Goldstein condition
    b0=al; a0=all; fb=f; gb=g; fa=f1; ga=g1;
    break,
end
% evaluate the directional derivative at alpha
eval(['h=' G '(x+al*s);']); g=h'*s;
if abs(g)<=-sigma*g0, % eq (2.5.6)
    a0=al; b0=al; done=1;
    break,
end
if g>=0, % going up the hill
    a0=al; b0=all; fb=f1; gb=g1; fa=f; ga=g;
    break,
end
if mu>(2*al-all),
% cubic minimization
m=[1 all all^2 all^3;1 al al^2 al^3;...
0 1 2*all 3*all^2;0 1 2*al 3*al^2];
c=rcond(m);
if c>1e-16,
    p=m\([f1 f g1 g]');
    r=roots([3*p(4) 2*p(3) p(2)]);
% stationary points of the cubic
    if abs((sin(angle(r(1))))>1e-15), % complex roots
% quadratic minimization
        m=[1 all all^2;1 al al^2;0 1 2*all];
        p=m\([f1 f g1]');
        if abs(p(3))>epsil,
            best=-.5*p(2)/p(3); % minimizer of the quadratic
        else
            best=0;
        end
    else % take the local minimizer of the cubic
        [v,q]=max(2*p(3)+6*p(4)*r);
        best=r(q);
    end
    c1=2*al-all; c2=min(mu,al+ftau1*(al-all));
% limits (see eq 2.6.2)
    oldbest=best;
    best=max(c1,min(best,c2));

```

```

        else % this condition should never occur!
            'problem with bracketing phase!'
            best=2*a1-all;
        end
    else
        best=mu;
    end
    fl=f; gl=g; all=a1; a1=best;
end
% test from eq. (2.6.3)
if (b0-a0)*ga<0 passed263=1; else passed263=0; end
a00=a0; b00=b0;
% sectioning phase
if (1-done),
    while 1,
        m=[1 a0 a0^2 a0^3;1 b0 b0^2 b0^3;...
           0 1 2*a0 3*a0^2;0 1 2*b0 3*b0^2];
        c=rcond(m);
        if c>1e-16,
% cubic interpolation
            p=m\([fa fb ga gb]');
            r=roots([3*p(4) 2*p(3) p(2)]);
            if abs((sin(angle(r(1))))>1e-15), % complex roots
% quadratic interpolation
                m=[1 a0 a0^2;1 b0 b0^2;0 1 2*a0];
                p=m\([fa fb ga]');
                if abs(p(3))>epsil,
                    al=-.5*p(2)/p(3);
                else
                    al=0;
                end
            else
                [v,q]=max(2*p(3)+6*p(4)*r); al=r(q);
            end
            c1=a0+ftau2*(b0-a0); c2=b0-ftau3*(b0-a0);
% limits (see eq. 2.6.4)
            al=max(c1,min(al,c2));
        else % this condition should never occur if passed263!
            if passed263
                'problems with sectioning phase! function too flat',
            end
        end
    end
end

```

```
        break
    end
    eval(['f=' F '(x+a1*s);']);
    eval(['h=' G '(x+a1*s);']); g=h*s;
    if (f>f0+rho*a1*g0) + (f>fa),
        gb=g; fb=f; b0=a1;
    else
        if abs(g)<=-sigma*g0, a0=a1; break, end
        if (b0-a0)*g>=0, b0=a0; fb=fa; gb=ga; end
        a0=a1; fa=f; ga=g;
    end
end
end
if fb>fa, result=a0; else result=b0; end
```

Appendix C

MATLAB Programs for Chapter 4

```
%
% =====
%
%           twodim.m
%
% =====
%
% This main program is implementing the data interpolation and noise
% filtering algorithms proposed in Chapter 4
%

clear
load pos1
bg=335; ed=550;
i=bg:ed;
X=north(i)-min(north(i))+50;
Y=east(i)-min(east(i))+50;
x1=ceil(min(X)/5)*5;    x2=floor(max(X)/5)*5;
y1=ceil(min(Y)/5)*5;    y2=floor(max(Y)/5)*5;
x12=x1:5:x2;
y12=y1:5:y2;
x1=length(x12);  y1=length(y12);
x12n=ones(y1,1)*x12;
y12n=y12'*ones(1,x1);
clear Dp
[s1 s2]=size(x12n);
thres=200;
df=50;
for i=1:1:s1,
for j=1:1:s2,
d1=X-x12n(i,j);
d2=Y-y12n(i,j);
d=sqrt(d1.^2+d2.^2);
[M 0]=sort(d);
```

```

pt=3;
O1=0(1:pt);
if max(O1)>thres,
Dp(i,j)=0;
else
x=d1(O1)/df;
y=d2(O1)/df;
f=depth(O1+bg-1);
Da=[ones(pt,1) x x.^2 y y.^2 x.*y];
a=pinv(Da)*f;
Dp(i,j)=-a(1);
end;
end;
end;
[sc1 sc2]=size(Dp);
wll=7; wlw=7;
% the nonlinear filtering processing window, the window size can
% be adjusted for the optimal processing effect. We found that
% window size of 7 by 7 gives us satisfactory results

y=[1:sc1*sc2];          % y is the vector for the serial numbers
x=reshape(y,sc1,sc2);   % rearrange the vector in a matrix form
z=x(1:wlw,1:wll);      % the serial number in the first block
y=reshape(z,1,wll*wlw)'; % rearrange the matrix in a vector form

an=sc1-(wll-1);        % an stands numbers of blocks in a row
bn=sc2-(wlw-1);        % bn stands numbers of blocks in a column
tn=an*bn;              % total numbers of blocks for processing
gp=y-1;                % starting vector recorded the serial number
for i=1:tn,
jj=rem(i,an)+an*(rem(i,an)==0);
% jj stands for increment index_1
% the increment index is the increment along the column axis for
% the blocks the next block along column direction is the serial
% numbers of previous + 1
kk=floor((i-1)/an);    % kk stands for increment index_2
% the increment index is the increment along the row axis for
% the blocks the next block along row direction is the serial
% numbers of previous + sc1

GP=gp+1*jj+sc1*kk;    % the serial numbers in the block

```

```
dp=Dp(GP);
% depth profile of the block

mn=mean(dp);
% mean value of the depth profile

st=std(dp);
% standard deviation of the depth profile

sigma2=0.04;
% noise variance that is found by the variance of the flat
% area that the depth profile is not very ragged and tough

Q=mean((dp-mn).^2)-sigma2;
if Q==-sigma2, kij=0; else kij=Q/(Q+sigma2); end;
center_index=GP((wll*wlw+1)/2);
lp=rem(center_index,sc1);
% if lp==0, lp=sc1; end;
wp=(center_index-lp)/sc1+1;
Dp1(lp,wp)=(1-kij)*mn+kij*Dp(center_index);
end;
figure(1)
contour(Dp);
figure(2)
contour(Dp1);
figure(3)
mesh(Dp);
figure(4)
mesh(Dp1);
V=[-1:-2:-35];
figure(1)
cs=contour(Dp,V);
figure(2)
cs=contour(Dp1,V);
```

VITA

Surname: Cheng

Given Names: Wei

Place of Birth: Taiwan

Date of Birth: October 23, 1968

Educational Institutions Attended:

University of Victoria, Victoria, B.C.	1992 to 1995
National Tsing Hua University, Hsinchu, Taiwan	1987 to 1991

Degrees Awarded:

B.Sc. National Tsing Hua University	1991
-------------------------------------	------

Honours and Awards:

Graduate Teaching Fellowship, University of Victoria	1993
Fellowship of English Language Program, UVic	1993
Taiwan Power Company Scholarship, Taiwan	1989 - 1991

Publications:

W. Cheng, W.-S. Lu, and A. Antoniou, "Efficient waveform decomposition on airborne laser bathymetry," *IEEE Pacific Rim Conference on Communication, Computers, and Signal Processing*, pp. 627-630, Victoria, B.C., May 17-19, 1995.

W. Cheng, W.-S. Lu, and A. Antoniou, "Noise filtering and enhancement of seabed topography for airborne laser bathymetry," *IEEE Pacific Rim Conference on Communications, Computers, and Signal Processing*, pp. 631-634, Victoria, B.C., May 17-19, 1995.

PARTIAL COPYRIGHT LICENSE

I hereby grant the right to lend my thesis to users of the University of Victoria Library, and to make single copies only for such users or in response to a request from the Library of any other university, or similar institution, on its behalf or for one of its users. I further agree that permission for extensive copying of this thesis for scholarly purposes may be granted by me or a member of the University designated by me. It is understood that copying of this thesis for financial gain shall not be allowed without my written permission.

Title of Thesis :

Depth-Estimation and Seabed-Visualization Techniques for Airborne Laser Bathymetry

Author:

Wei Cheng

August 23, 1995